2024

Quasi-static and dynamic tension testing of as-built and heat-treated additively manufactured 316L stainless steel

Terrell Elias Marler

QUASI-STATIC AND DYNAMIC TENSION TESTING OF AS-BUILT AND HEAT-TREATED ADDITIVELY MANUFACTURED 316L STAINLESS STEEL

Terrell Elias Marler

A THESIS

Submitted in partial fulfillment of the requirements
for the degree of Master of Science
in
Mechanical Engineering
to
The Graduate School
of
The University of Alabama in Huntsville
May 2024

Approved by:

Dr. Nathan Spulak, Research Advisor & Committee Chair
Dr. Nicholas Ginga, Committee Member
Dr. Judith Schneider, Committee Member
Dr. George Nelson, Department Chair
Dr. Shankar Mahalingam, College Dean
Dr. Jon Hakkila, Graduate Dean

Abstract

Quasi-Static and Dynamic Tension Testing of As-Built and Heat-Treated Additively Manufactured 316L Stainless Steel

Terrell Elias Marler

A thesis submitted in partial fulfillment of the requirements for the degree of Master of Science

Mechanical Engineering

The University of Alabama in Huntsville
May 2024

Additive manufacturing (AM) has several advantages over conventional subtractive manufacturing techniques, including the ability to create parts of highly complex geometries in one process thus reducing time and cost for each part. However, AM parts show different mechanical behavior compared to wrought parts due to the differences in the manufacturing processes. In particular, lack-of-fusion defects, voids, and keyhole defects can act as crack initiation sites leading to the possibility of more brittle behavior. This may be exacerbated by high rate loads, which tends to induce more brittle behavior, higher flow stress, and higher yield stress in materials. Therefore, it is critically important to characterize the material at the strain rate it will experience during use, for example in the automotive industry where the AM parts will experience dynamic loading during crash events. In this study, tension tests are performed on AM 316L stainless steel at strain rates of $10^{-3}\ s^{-1}$, 1000 s^{-1}, 2500 s^{-1}, and 5000 s^{-1}, and results are compared to conventional wrought 316L. The experimental results are used to develop a material model for finite element analysis using LS-DYNA. The microstructure in the samples are then examined.

Acknowledgements

First, I would like to thank my parents, Brad and Carleigh Marler, who always supported me through anything and who are always willing to take a phone call. I would like to also thank my brothers, Ezra and Zuri, who have always been great friends, company, and support. My family always has been incredibly supportive and loving, and I will always be grateful. I would like to thank my wonderful girlfriend, Rachel Hollings. She has always been willing to spend time with me when I was stressed out. My friends have also been very instrumental in my life: Atherton Mook, Hays Mook, Jackson Collette, Nick Perlaky, and Zach Thornton, and I cannot thank them enough for all they have done.

I would like to thank Dr. Nathan Spulak for always giving me guidance, always answering my questions, helping me work on my thesis, and supporting my research financially. I will always be thankful for the help. I would also like to thank my lab mates, Derryk Daignault, Abigail Schauer, and Sydney Resnick, who helped me work through homework and who always had fun conversations in the lab. I would also like to thank the Quadrus Corporation, who printed the parts used in this study.

Table of Contents

List of Figures

List of Tables

List of Acronyms

Acronym	Description
L-PBF	Laser-Powder Bed Fusion
HIP	Hot Isostatic Press
AM	Additively Manufactured
SHB	Split-Hopkinson Bar
SR	Strain Rate
DIC	Digital Image Correlation
FEA	Finite Element Analysis
AM316L	Additively Manufactured 316L Stainless Steel
HT	Heat-Treated
AB	As-Built
SR	Strain Rate
fps	Frames per Second
OM	Optical Microscopy
SEM	Scanning Electron Microscope

Chapter 1. Introduction

Additive manufacturing (AM) is a different manufacturing process than conventional methods of manufacturing. The newer process allows for one step production of parts on one machine, but this comes with some drawbacks. The new manufacturing methods come with new material properties, and they must be investigated before the new additively manufactured parts become widely used. In specific, strain rate sensitivity can be hard to quantify. A split-Hopkinson bar and a hydraulic load frame are used to quantify and determine the material properties of AM 316L stainless steel in an as-built condition, where no heat treatment is applied after being manufactured, and in a heat-treated condition, where a homogenization heat treatment is applied to the specimens after manufacturing. The results are used to create stress vs. strain curves to visualize the strain rate sensitivity, and they are also used to create a Johnson-Cook model to quantify the strain rate sensitivity and accurately create a stress vs. strain curve for any given strain rate. The quasi-static results are then input into LS-DYNA to create a material model for finite element simulations to predict material response. Lastly, microstructural analysis is done on the grip section of used test samples to view the effect of heat treatment.

Chapter 2. Background and Literature Review

2.1 Material Testing

Mechanical testing of materials is a common practice to determine how the material will respond to loads and deformation. A common mechanical test for materials is a tension test, which gives the force response of a material at certain displacements. Engineering stress vs. strain curves can be created from these forces and displacements to normalize the data relative to the geometry of the specimen. This is calculated using Equations (2.1) and (2.2):

$$\sigma_e = \frac{F}{A_0}, \tag{2.1}$$

$$\epsilon_e = \frac{\Delta L}{L_0}, \tag{2.2}$$

where σ_e is engineering stress. F is force, A_0 is original cross-sectional area, ϵ_e is engineering strain, L_0 is original length, and ΔL is change in length.

These engineering stress and engineering strains can be converted to true stress and true strain. The benefits of converting from engineering values is that the true values adjust themselves for the changing geometry of the sample as they undergo deformation. Using the assumptions that the volume is conserved and that the sample has a constant cross-sectional area (a valid assumption until necking), the true stress value takes into account the changing cross-section of the sample. Similarly, the true strain takes into account the changing length of the sample as it is deformed. For example, if the cross-section shrinks

due to a strain on the sample and the Poisson effect, but the force through the sample stays constant, the engineering stress stays constant, but the true stress increases. To convert from engineering stress and strain to true stress and strain the following formulas are used:

$$\epsilon_{true} = ln(1 + \epsilon_e)\,, \tag{2.3}$$

$$\sigma_{true} = \sigma_e(1 + \epsilon_e) = \sigma_e \times \exp(\epsilon_{true}), \tag{2.4}$$

where σ_{true} is the true stress, σ_e is the engineering stress, ϵ_{true} is the true strain, and ϵ_e is the engineering strain.

Strain rate is the rate at which strain is applied. The true strain rate is calculated as follows:

$$\dot{\epsilon}_{true} = \frac{\dot{\epsilon_e}}{1+\epsilon_e}\,, \tag{2.5}$$

where $\dot{\epsilon_e}$ is the engineering strain rate, and $\dot{\epsilon}_{true}$ is the true strain rate.

Tension testing can be done at low or high rates to determine material properties for any applicable load case. High rate or dynamic tension testing is a method of determining material response when strain is very quickly induced in a material. Materials may show changes in ultimate stress, yield stress, and/or fracture strains when loaded at different strain rates as demonstrated in Figure 2.1.

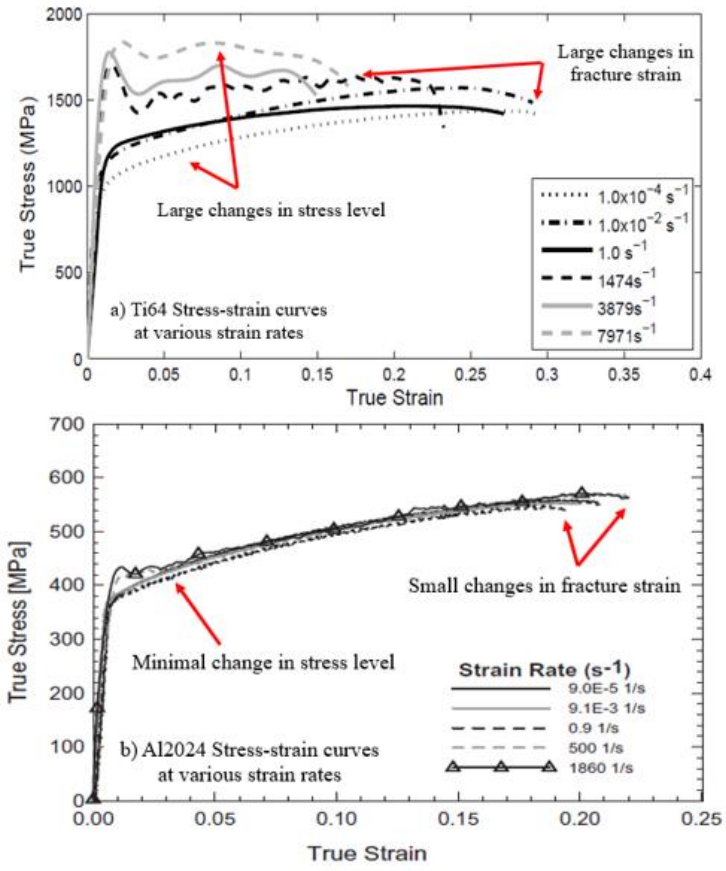

Figure 2.1: Mechanical Response of a) Titanium 6Al-4V (Hammer 2012) and b) Aluminum 2024 (Seidt and Gilat 2013) when loaded over a wide range of strain rates.

Figure 2.1 shows 2024 aluminum to be less strain rate sensitive than Titanium 6Al-4V due to the greater decrease in fracture strain and the greater increase in stress levels across various strain rates in Titanium 6Al-4V than in 2024 aluminum.

Figure 2.2 below shows numerous different experimental techniques at the various strain rates achievable using each technique. Conventional hydraulic or screw-driven load frames are capable of testing at low strain rates between $10^{-5}\ s^{-1}$ and $1\ s^{-1}$. They are typically unable to achieve results at higher strain rates due to the limited response time of the control system.

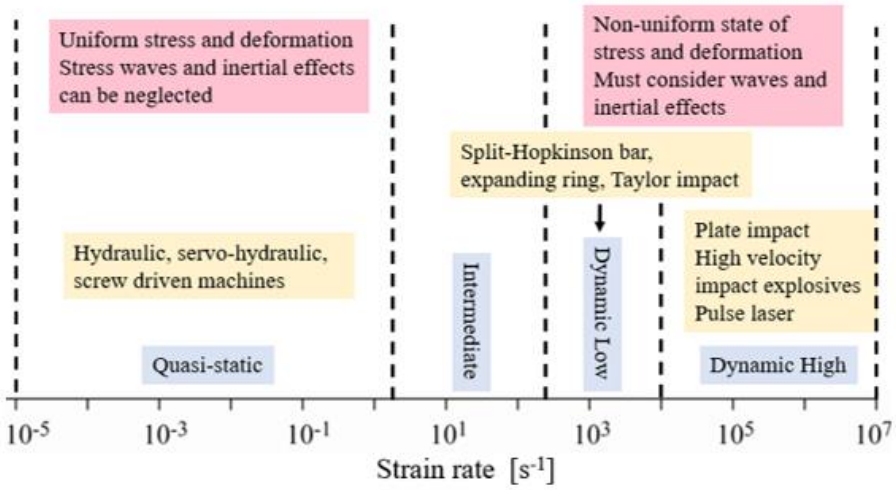

Figure 2.2: Summary of different mechanical characterization experimental methods and the possible strain rates capable of being achieved using each method.

Experimental techniques capable of achieving strain rates in the dynamic low regime (~$10^3\ s^{-1}$ to $10^4\ s^{-1}$) include expanding ring, Taylor impact, and split-Hopkinson bar (SHB). The expanding ring setup consists of explosives placed in the center of a ring, which expands on detonation, and a stress vs. strain curve is created (Hoggatt and Recht 1969). This technique works for high strain rates up to $10^5\ s^{-1}$, but it requires assumptions to find an estimate of material strength from the velocity that the ring expands. This method also only measures the material response under tensile loads. Another technique for measuring dynamic effects of a material is the Taylor impact, where a sample is shot against an anvil or hard surface, and the distance that the plastic compression wave travels backwards down the sample is used to find the ratio of dynamic yield stress to static yield stress (Taylor 1969). This method requires few pieces of specialized equipment and provides a good estimate for dynamic yield stress but gives no extra information about the material such as flow stresses and only allows compression tests. The SHB technique allows for direct measurement of both the stress and strain and construction of full stress vs. strain curves up until the point of fracture in tension, compression, and shear. However,

it requires a large setup, which includes two long bars on either side of the sample to capture the strain waves traveling on both sides of the sample. Strain gauges attached to each bar on either side of the sample can use the known bar properties to determine the force in the sample. The split-Hopkinson bar is also limited to the $10^3\ s^{-1}$ regime, however, without a specialized setup.

2.2 Split-Hopkinson Bar Testing

Hopkinson (1914) used elastic waves in rods as a method of measuring the momentum of bullets fired at a rod of similar properties. On the end opposite the impact, a secondary rod is attached that is held together magnetically with enough force to hold it together but not enough to impact the momentum readings. As the pressure wave induced by the bullet hits the free end of the secondary bar, the compression wave reflects to form a tension wave travelling in the opposite direction. This breaks the magnetic force, and the secondary bar flies off into a box where the momentum is trapped inside and measured. Hopkinson then shows that the pressure in the bar is equal to λv_0^2, where $\lambda = \lambda(x)$ and is the mass per unit length of the bullet and is the variable used by Hopkinson, and v_0 is the impact velocity to create a pressure curve.

Kolsky in 1949 developed the split-Hopkinson bar (SHB) testing device based on Hopkinson's work in the field of dynamic wave behavior. The split-Hopkinson bar used a detonator to propel the anvil, which was attached to an incident bar. As the wave travels down the bar, the wave would pass by an inertia switch, which triggered the strain gauges that Kolsky used. He measured the incident, reflected, and the transmitted wave, which is the wave created from the impact from the striker bar, the wave reflected off of the back of the specimen as the wave attempts to traverse it, and the wave that transmitted through the

sample, respectively. These principles are the idea behind the modern split-Hopkinson bar, which is used to conduct the higher strain rate experiments in this report.

The split-Hopkinson Bar (SHB) is a test setup for measuring dynamic behavior of materials that includes 4 main parts: a pressure vessel, a striker bar, a transmitter bar, and an incident bar. The pressure vessel accelerates the striker bar into the incident bar, which generates an elastic wave that travels down the bar towards the sample, which sits between the incident and the transmitter bars. As the wave meets the sample, a portion of the wave is reflected back in the opposite direction in the incident bar, and the remainder of the wave is transmitted through the specimen and into the transmitter bar. These waves are all captured by strain gauges on both the transmitter bar and the incident bar. For a tension setup, a hollow striker bar that has an inner diameter that is the same as the incident bar's outer diameter is fitted around the incident bar, and a flange is screwed into the back of the incident bar. The pressure gun, facing away from the sample, fires the hollow striker bar into the flange of the incident bar, which creates the incident wave in tension. For a compression setup, the pressure gun is flipped around such that the striker is fired directly into the incident bar, as shown in Figure 2.3.

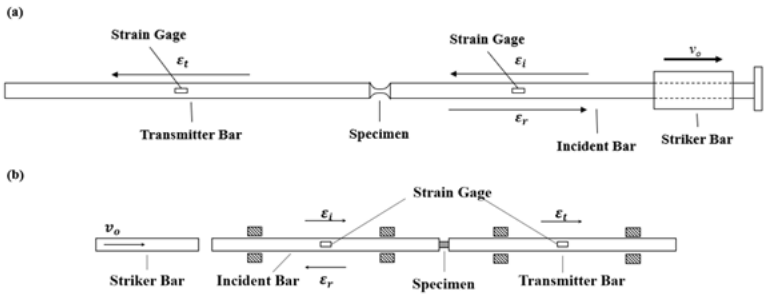

Figure 2.3: Schematic of (a) tension SHB and (b) compression SHB experimental setup.

The wave caused by the impact of the striker bar with the incident bar is called the incident wave, the wave that is reflected back at the sample is called the reflected wave, and the wave that makes it through the sample is called the transmitted wave. Sample wave data is shown in Figure 2.4.

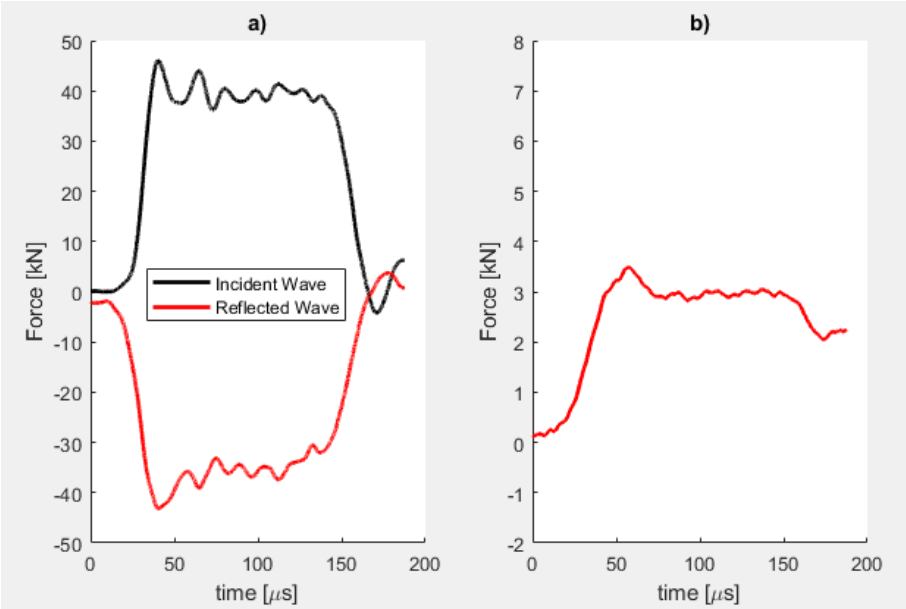

Figure 2.4: Sample wave data recorded from strain gauges on the incident (a) and transmitter bars (b).

Figure 2.4 shows sample data from a tension setup, which is where the incident and transmitted waves are in tension and the reflected wave is in compression. However, compression setups would have the reverse, where the incident and transmitted waves are in compression and the reflected wave is in tension. Torsional setups also exist to test materials in torsion at high strain rates (Gilat 2000).

The strain in the bar is correlated to the velocity at that location on the bar. So, as the strain wave is traveling through the bar, the segment experiencing strain is the only part that is moving. To convert from strain to velocity at the end of the bar, Equation (2.6) is used:

$$\epsilon_{\text{bar}} = \frac{v}{2c_b}, \tag{2.6}$$

where ϵ_{bar} is the strain experienced by the strain gauge, v is the velocity at the point experiencing the strain, and c_b is the wave speed of the metal in the bar. The wave speed is calculated using Equation (2.7):

$$c_b = \sqrt{\frac{E}{\rho}}, \tag{2.7}$$

where E is the elastic modulus (Young's modulus) of the bar, and ρ is the density of the bar, and c_b is the wave speed in the bar.

To find the engineering strain rate across the bar, the velocity measurements from strain gauges are subtracted to find the specimen change in length, which is then divided by the original length as follows:

$$\dot{\epsilon}_e(t) = \frac{v_i(t) - v_t(t)}{L_s} = \frac{2c_b(\epsilon_i - \epsilon_t)}{L_s} = \frac{2c_b\epsilon_r(t)}{L_s}, \tag{2.8}$$

where $v_i(t)$ and $v_t(t)$ are the velocities of the incident and transmitter bars, respectively, L_s is the length of the sample, c_b is the elastic wave speed in the bar, and $\epsilon_r(t)$, $\epsilon_i(t)$, and $\epsilon_t(t)$ are the strain in the reflected wave, the strain in the incident wave, and the strain in the transmitted wave, respectively. This shows that the reflected wave is proportional to the strain rate. To solve for strain in the sample, the strain rate is integrated:

$$\epsilon_e(t) = \int_{t_i}^{t_i+t} \left(\dot{\epsilon}_e(t)\right) dt, \tag{2.9}$$

where t_i is the time where the impact occurs, and ϵ_e is the engineering strain in the sample (Seidt 2010).

Stress data can be recorded on the split-Hopkinson bar using the transmitter bar by doing what is called a "1-wave analysis." The force recorded in the transmitter bar is equivalent to the force exerted on the bar by the back of the sample. This force is also the

portion of the wave that is able to pass through the sample. This is shown in Equations (2.10) & (2.11):

$$F_{sample}(t) = A_{bar}E_{bar}\epsilon_t(t), \tag{2.10}$$

$$\sigma_{\text{sample}}(\text{t}) = \frac{A_{bar}E_{bar}\epsilon_t(t)}{A_{sample}}, \tag{2.11}$$

where σ_{sample} is the stress in the sample, A_{sample} is the cross-sectional area of the sample, $F_{sample}(t)$ is the force in the sample measured from instant when force reaches the sample, A_{bar} is the cross-sectional area of the bar, E_{bar} is the elastic modulus of the bar.

However, this is not completely accurate as an analysis technique because this assumes dynamic equilibrium, which is where the force on one side of the sample is equal to the force on the other side of the sample. Generally, at the beginning of the test, the sample undergoes a "ringing-up" phase. This is where the waves bounce back and forth inside the sample itself until it finds an equilibrium. The "ringing up" phase is why a 2-wave analysis proves useful. Comparison between the 1-wave and 2-wave analysis is used to determine whether or not the sample is in dynamic equilibrium by verifying that the force is the same on either side of the sample. The 2-wave analysis involves summing the reflected wave and incident wave to find the force on the incident bar by the sample. If the forces are the same on either side of the sample, it is in dynamic equilibrium. Equation (2.12) shows how the force on either side of the sample can be compared. If Equation (2.12) experimentally holds true, the sample is considered to be in dynamic equilibrium (Seidt 2010):

$$\sigma_{\text{sample}}(\text{t}) = \frac{A_{bar}E_{bar}\epsilon_t(t)}{A_{sample}} = \frac{A_{bar}E_{bar}\left(\epsilon_i(t)+\epsilon_r(t)\right)}{A_{sample}}, \tag{2.12}$$

where $\epsilon_t(t)$ is the strain in the transmitter bar measured from the start of the wave, $\epsilon_i(t)$ is the strain in the incident wave from the start of the wave, and $\epsilon_r(t)$ is the reflected wave also measured from the start of the wave.

2.3 Additive Manufacturing

Additive manufacturing is a more modern technique than traditional subtractive manufacturing. Subtractive manufacturing is the typical lathing, milling, and cutting operations, used to remove unwanted material from a larger workpiece. Additive manufacturing is where material is added, layer-by-layer. This typically involves some type of feedstock and a heat source to melt the feed stock where additional material is required in the overall part. Different variations of feedstock and heating source will change the build speed, build accuracy, material efficiency, part cost, and safety issues (Garcia-Colomo, *et al.* 2020). The heating techniques range from using a laser (photons) to a beam of electrons as a heating source, and the feedstock is generally wire or powder. A breakdown of the AM techniques is shown in Figure 2.5.

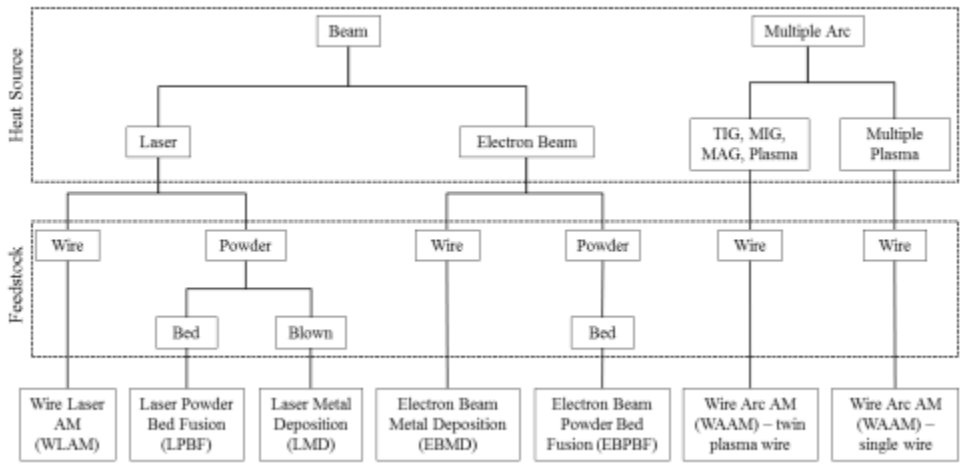

Figure 2.5: Additive manufacturing techniques (Garcia-Colomo *et al.* 2020).

Despite there being many types of additive manufacturing techniques, the one that has been selected for this project is Laser Powder Bed Fusion (L-PBF). L-PBF has been selected due to its resolution of small features ($\pm$ 0.04 mm) relative to the other processes (Ding *et al.* 2015). The drawbacks include slow build rates relative to other AM processes and low overall energy efficiency of 2%-5% (Ding *et al.* 2015). L-PBF is a process where a bed of powder with powder diameter ranging from 10 μm to 40 μm is laid over the surface of the sample that is being built, and a laser selectively melts the powder to build the part up in layers. Factors that affect material properties are laser path (scan strategy), laser power (P), scan speed (v), layer thickness (t), and hatch spacing (h). These parameters can be collapse into an energy density (E) of the part, $E = \frac{P}{vht}$. These properties must first be optimized for each material such that the relative density, or the density of the AM part relative to the density of the wrought material, of the sample will be >99% (Liu *et al.* 2021).

The operating window of this process is primarily a function energy density of the build process. Too low of an energy density, and the result is not all of the powder will melt, creating pockets of unmelted powder inside of the AM part and leading to a porosity of the material that hot isostatic pressing (HIP) cannot fix (Rodrigues *et al.* 2023). Too high of an energy density, and keyhole formation may occur. Keyhole formation is where the energy is so high that vaporization occurs. The defect looks similar to a keyhole, which is shown in Figure 2.6.

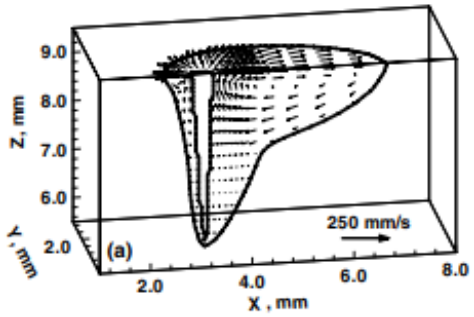

Figure 2.6: Keyhole formation is 304L SS (Rai *et al.* 2007).

As the power and the scanning speed of the laser increase, balling will occur. Balling is where the material clumps up with itself instead of solidifying in a line like it is intended to. Balling creates issues when a new powder layer is deposited on top of the balled layer, and the previous layer is not flat as expected. It can cause porosity and potentially delamination of the layer (Gu and Shen 2009). Figure 2.7 shows the degrees of balling that can occur as energy density is kept constant, but laser speed and wattage are increased together in 316L stainless steel.

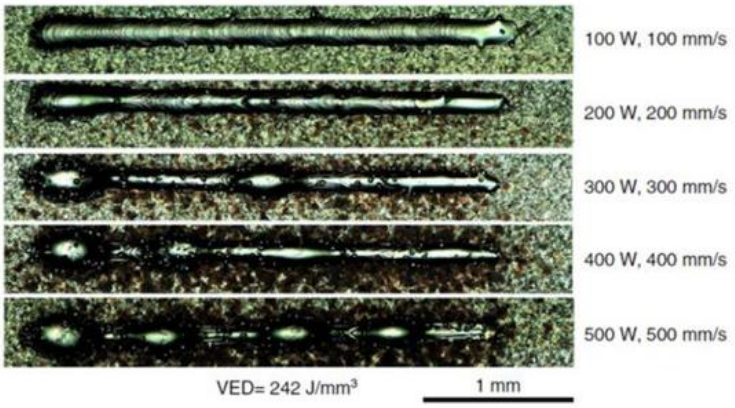

Figure 2.7: Degrees of balling of 316L SS (Ahmed *et al.* 2022).

2.4 Digital Image Correlation

Digital image correlation (DIC) is an optical technique to measure displacements and to calculate the resultant strains on a deforming body. The specimen is first painted with a

speckle pattern. The technique works by using software to analyze pictures taken of the sample throughout the test. The camera takes images, and each pixel is given a darkness value from 0 to 255, and breaks the speckle pattern into subsets. The DIC software then "follows" each subset on the sample to find the displacements at each point. The software can calculate full-field user-selected strain tensors (Lagrange, Euler, Hencky, etc.) across the sample using the displacement measurements by removing the rigid body motion. This is useful because in tension, necking can occur, creating localized strains much higher than the average strain, extensometer strain, or strain calculated by the overall displacement measured at the grips. Additionally, a virtual extensometer can be placed on the sample to isolate elongation of just the gauge section in tensile specimens as shown in Figure 2.8.

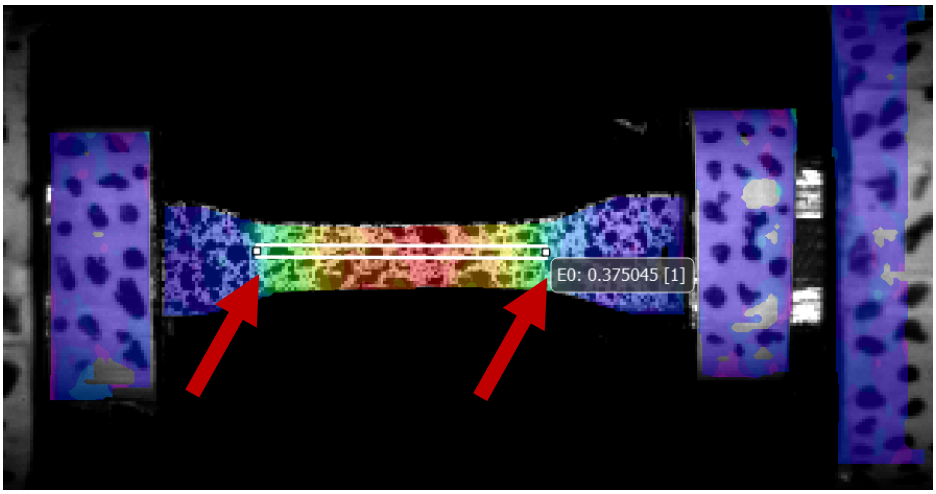

Figure 2.8: DIC Data of a 316L stainless steel sample with axial Hencky strain as the contour plot and virtual extensometer endpoints shown with arrow.

2D and 3D DIC are both used to ensure accurate measurements. The 3D DIC is generally more accurate due to the ability to track out-of-plane displacements, while 2D DIC is limited to in-plane displacement.

Local point strains are "averaged" across a small length, which can be represented by the virtual strain gage length (VSGL). The DIC localized point strains are analogous to

placing small "virtual" strain gauges across the sample, and the length of these virtual strain gages are determined using Equation (2.13):

$$VSGL = \frac{mm}{pixel} \times step \times filter\,, \tag{2.13}$$

where $VSGL$ is virtual strain gage length in mm, $\frac{mm}{pixel}$ is experimentally determined by taking a picture of a ruler in 2D and taking many pictures of a calibration panel in 3D, $step$ is an integer selected in post-processing related to how many pixels are skipped over to check for the next one, and $filter$ is an integer greater than 5 selected in post-processing related to the number of subsets that the motion of the target subset is compared to to eliminate rigid body motion and compute strain. As the camera resolution increases, the $\frac{mm}{pixel}$ decreases. This means that camera resolution is inversely related to the $VSGL$.

Using DIC, strain at the necking point as opposed to extensometer strain over the whole sample can be calculated. When necking onsets in a material undergoing a tension test, the true stress and true strain mathematical conversions in Equations (2.3) & (2.4) are no longer applicable, and attempting to use these equations to calculate the true stress and true strain post-necking typically results in a decreasing value of the true stress as true strain increases. However, this is generally not the actual behavior of the metal, and the actual localized strain of the necking point can be used instead to calculate the true stress past necking. The Hencky strain tensor, calculated as $\epsilon_H = \ln(F^T F)$, where F is the deformation gradient, can to be used to find the strain at a point, due to the Hencky strain tensor being considered a "true" strain (as opposed to an engineering strain) (Onaka 2012). Before the point of necking, the Hencky strain at the necking point (or anywhere else on the sample) is the same or generally very close to the mathematically converted true strain found using the extensometer (engineering) strain. After the point of necking, local Hencky

strain in the necked region increases beyond the value calculated using the extensometer strain. Stress vs. strain curves where the axial DIC Hencky strain is used instead of the true strain to find true stress from Equation (2.4) result in a slightly modified and in some cases more useful stress vs. strain curve in that before necking, the DIC Hencky true stress vs. true strain curve is very similar to the extensometer true stress vs. true strain curve, but after necking, the stress values in the DIC Hencky true stress vs. true strain curve increase beyond the stress values of the extensometer true stress vs. strain curve. Using this DIC Hencky strain generally also allows stress vs. strain curves to remain monotonically increasing even after necking. The Hencky strain tensor stress vs. strain curves are useful for a material model in finite element analysis (FEA) simulations.

Figure 2.9 shows how using local DIC Hencky strain as the value for true strain and reconverting the engineering stress to true stress in accordance with Equation (2.4) creates a new stress vs. strain curve when compared to the traditional extensometer stress vs. strain curves.

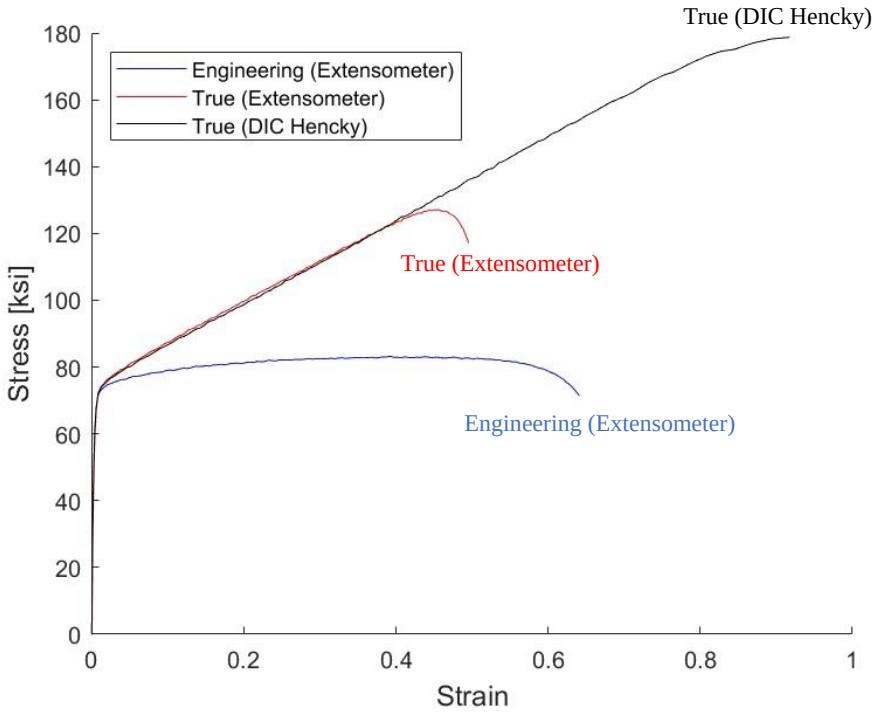

Figure 2.9: Differences in stress & strain calculations (AM316L-AB-SR1-N1).

2.5 Finite Element Analysis

The tests are simulated using finite element analysis (FEA), and the DIC fail point Hencky strain is used to construct a material model for each material. The Hencky stress vs. strain curve is input into the material model, and when the FEA element size is similar to or smaller than the VSGL, this curve will be representative of the material with few changes.

Current common practice for determining material model stress vs. strain curves past necking involves a method where a stress vs. strain curve is truncated at the point of necking, and a "fan" of curves are appended to the end of the truncated curve, as shown in Figure 2.10.

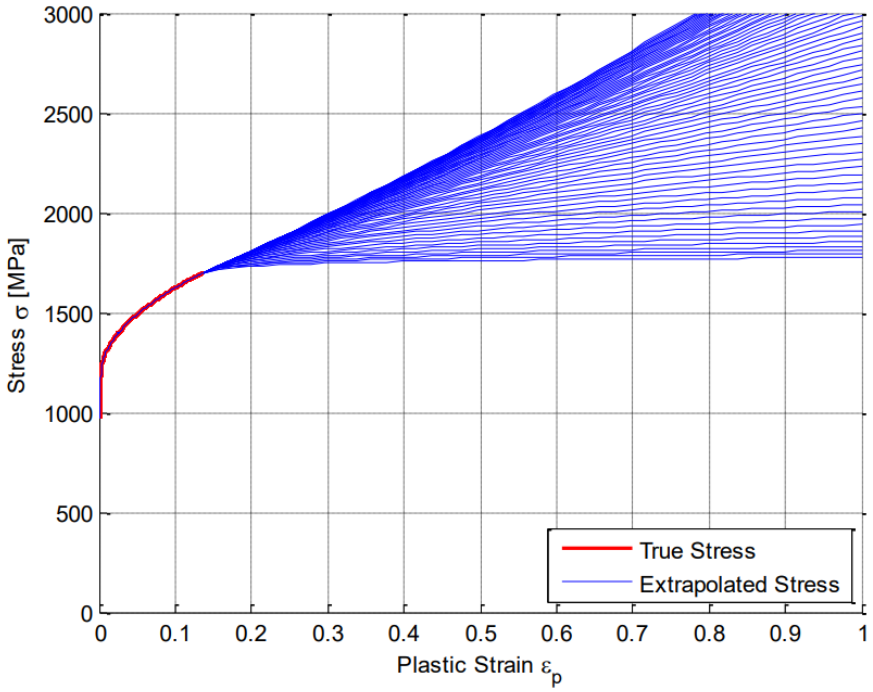

Figure 2.10: "Fan" method for determining stress vs. strain behavior post-necking (Dolci *et al.* 2016).

Each of the curves are used as a material model in a finite element simulation with an extensometer and the load across the cross-section of the FEA-modeled sample being measured and recorded. After each simulation, the force vs. displacement curve from the simulation is compared to the actual material response, and the material model that is closest to the experimentally observed response is selected. This is shown in Figure 2.11, which shows FEA simulations using two different material model curves compared to the actual material response.

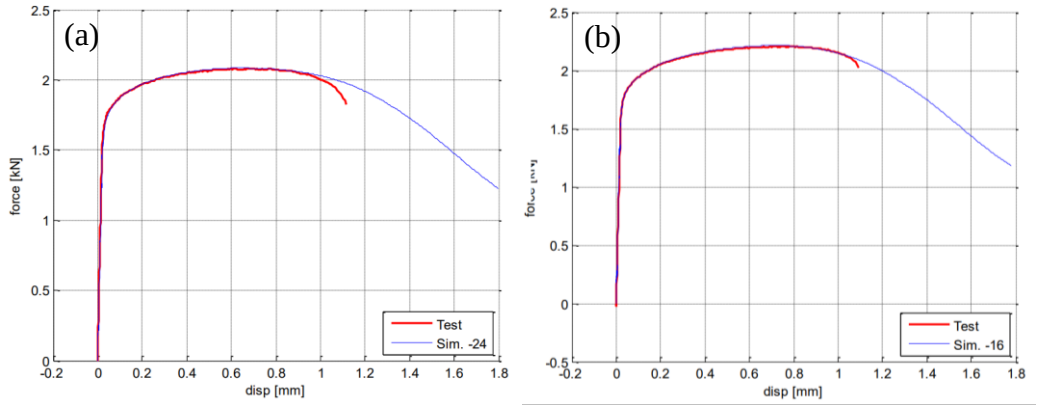

Figure 2.11: Different fits for different material models: Sim 24 (a) is a much poorer fit to the actual response than Sim 16 (b) (Dolci *et al.* 2016).

Figure 2.11 shows that Sim 16 (Figure 2.11b) is a better fit, so in this case, Sim 16 (Figure 2.11b) will be selected over Sim 24 (Figure 2.11a). The material model stress vs. strain curve is truncated such that the final strain is the strain at fracture.

The Johnson-Cook (JC) material model is used to assign parameters to observed behavior of materials. It is designed to quantify strain rate sensitivity, temperature sensitivity, and to predict the plastic region behavior of the material for use in material modeling in FEA or easy quantification of material properties. A popular form is as follows:

$$\sigma = [A + B(\epsilon^p)^n]\left[1 + Cln\left(\frac{\dot{\epsilon}}{\dot{\epsilon}_o}\right)\right]\left[1 - \left(\frac{T - T_r}{T_m - T_r}\right)^m\right], \tag{2.14}$$

where A is the yield stress, B is the hardening modulus, n is the hardening coefficient, C is the JC strain rate sensitivity coefficient, and m is the JC temperature sensitivity coefficient, and these are fitted parameters; ϵ^p is the plastic strain, $\dot{\epsilon}$ is the strain rate, $\dot{\epsilon_0}$ is the reference strain rate, T is the temperature of the test, T_r is the reference temperature, and T_m is the melting temperature of the material (Johnson & Cook 1985) (Umbrello *et al.* 2007).

A, B, and n are calculated by fitting a power law hardening to the reference strain rate and reference temperature data. Once they are found, C, the strain rate sensitivity

parameter, is found by using the stress at a set strain value for various strain rates and fitting the most accurate C value to that set of data. To find m, the strain rate is kept constant at the reference strain rate, and the stress values at the same set strain value as was used for finding C are found and the value for m that best fits the data is selected.

C is generally regarded as the JC strain rate sensitivity parameter, and prior researchers determined that for AM 316L Stainless Steel, this value is 0.013 to 0.018 (Güden *et al.* 2022). The value for C is likely dependent on processing parameters used in the AM process, and different processing may yield different values for C.

2.6 Heat Treatments

HIP is a process where a combination of heat and pressure (isostatic pressing) lead to a reduction of internal porosity in the microstructure. In the as-built condition for L-PBF, relative density can be up to around 99% for 316L Stainless Steel, and the grains are often columnar. However, after the HIP process at 1100 °C for 3 hours in a 99.5% argon atmosphere at a pressure of 150 MPa, the relative density can get up to 99.8% or higher, and the grains generally become equiaxed and appear as if the material is in its original annealed condition for 316L stainless steel (Rodrigues 2023). The high-pressure conditions are to ensure the closure of air pockets that are not exposed to air. Air pockets that are open to the exterior will not be affected by HIP. In the porosity regions inside the material, the gas trapped inside the material can diffuse into the metal under the hot, high pressure conditions, and can diffuse to the outside of the material depending on the diffusivity of the gas, decreasing porosity (Atkinson and Davies 2000).

Stress relief is a heat treatment with heat being applied to sample that requires an increase in temperature to a temperature where the dislocations within the material gain

mobility and are able to organize into subboundaries to create a more uniform internal stress distribution without changing the material properties. A typical stress relief in 316L is 650 ℃ for 2 hours (Dossett and Totten 2013). The process when conducted on additively manufactured 316L stainless steel by Gel'atko *et al.* (2023) shows that 6 hours at 650 ℃ reduces internal stresses from an average internal normal stress of 119.7 MPa to -16.84 MPa.

Homogenization is another heat treatment that is done at a higher temperature and often more time than stress relief with the objective of refining the grains, so that grains can become more equiaxed, and the material can become more isotropic. Homogenization also minimizes any elemental segregation resulting from solidification. To successfully homogenize a 316L stainless steel, 1050°C to 1200°C for 2 hours should be generally be effective (Dossett and Totten 2013). Gel'atko *et al.* (2023) also shows major improvements in grain structure from a columnar AM structure to a very homogenized grain structure in Figure 2.12. Although this study was at a lower temperature, the longer time resulted in grain changes.

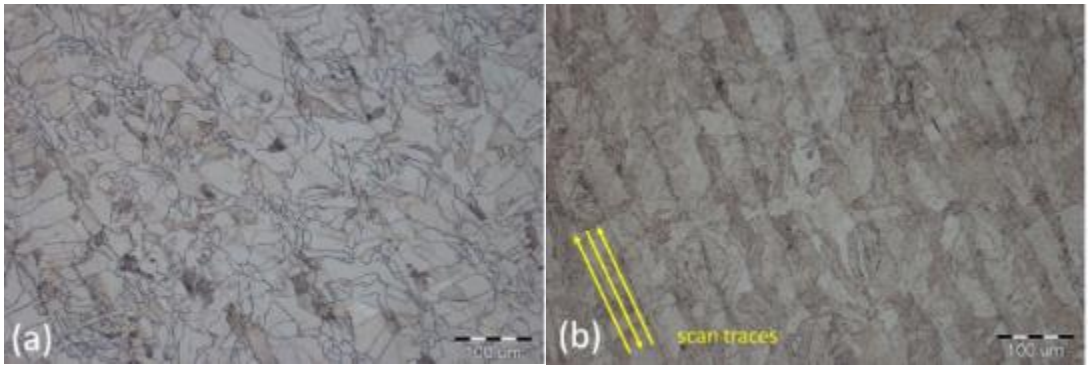

Figure 2.12: (a): After homogenization heat treatment at 750 ℃ for 8 hours, (b): Before homogenization in AM316L SS (Gel'atko 2023).

To view the effect heat treatments in the microstructure of the sample, a process of grinding, polishing, and etching must be completed. The grinding process begins with the

sample being cut to show a cross-section and mounted in a molding compound to allow the sample to be gripped by the mount instead of on the sample. After mounting, the sample is grinded with water to reduce the damage from the cutting process. The grinding process is repeated using finer and finer sand paper to reduce scratches from cutting. After grinding the surface of the sample, a finer polishing process is done to further reduce the scratch damage from the sand paper. Polishing is done using a polishing cloth, a fine abrasive powder, and water. Common abrasives include diamond, aluminum oxide, and colloidal silica, and common polishing cloth types include woven nylon, flocked rayon, synthetic textile, and polyurethane pad (Schneider 2023). The grinding and polishing steps are shown in Figure 2.13.

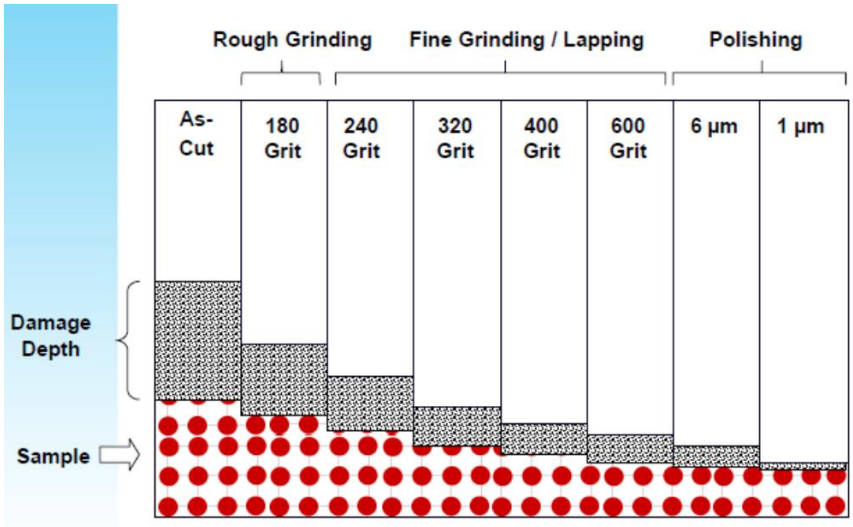

Figure 2.13: Grinding and polishing process visually reducing damage depth in sample (Schneider 2023).

After sufficient polishing, the particulate size of the powder is reduced to further polish the sample and remove the finest scratches in the surface. The microstructure is potentially visible under an optical microscope after this process. To further reveal the microstructure, and etching process is utilized. The etching process where a polished surface of a metal is exposed to an etchant specific to the material is used and will reveal

the microstructure. Common etchants include Keller's Etch on aluminum alloys, Kroll's Reagent on titanium, Nital on carbons steels, and Kallings Reagent on stainless steels (Schneider 2023)

Chapter 3. Experimental Procedures and Techniques

3.1 Specimen Design and Material

The selected material is AM 316L stainless steel. 316L stainless steel is an alloy of steel modified from the 304 Series Stainless Steel with low carbon and high molybdenum to have good weldability but also high chemical resistance to corrosion, respectively. The L stands for low carbon. Table 3.1 below shows the chemical composition of relevant steels.

Table 3.1: Elemental Composition of Relevant Steels (ASTM Standard A240/A240M).

Type	C	Mn	P	S	Si	Cr	Ni	Mo	N	Cu	Fe
304L	.030	2.00	.045	.030	.75	18.0-20.0	8.0-12.0	0	.10	0	Bal.
316	.08	2.00	.045	.030	.75	16.0-18.0	10.0-14.0	2.00-3.00	.10	0	Bal.
316L	.030	2.00	.045	.030	.75	16.0-18.0	10.0-14.0	2.00-3.00	.10	0	Bal.
317L	.030	2.00	.045	.030	.75	18.0-20.0	11.0-15.0	3.00-4.00	.10	0	Bal.

Tension specimen geometry is shown in Figure 3.1. The specimens have a gauge length of 7.62 mm, 1.52 mm in thickness, and 2.79 mm in width.

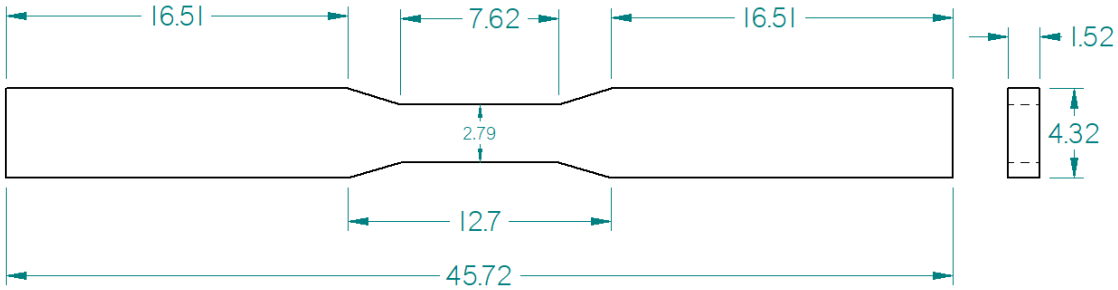

Figure 3.1: Specimen geometry with dimensions in mm.

The technique used to additively manufacture the specimens is Laser Powder Bed Fusion using a GE Concept Laser MLab in an argon environment with a power of 100W a scan speed of 802 mm/s, a hatch spacing of 59.25μm, and a layer thickness of 25 μm for an energy density of $E = \frac{P}{vht}$ =84.2$\frac{J}{mm^3}$, where E is energy density, P is laser power, v is the scanning speed, h is the hatch spacing, and t is the layer thickness. This should lead to a part relative density of >98.5% (Choi *et al.* 2016). The parameters were determined using vendor best practices, and the parts are manufactured on a steel plate. Thirty samples are manufactured and numbered. Samples 1-15 are heat-treated at 1950 °F for 5 hours in an

argon environment and furnace cooled. The build plate and sample location are shown in Figure 3.2.

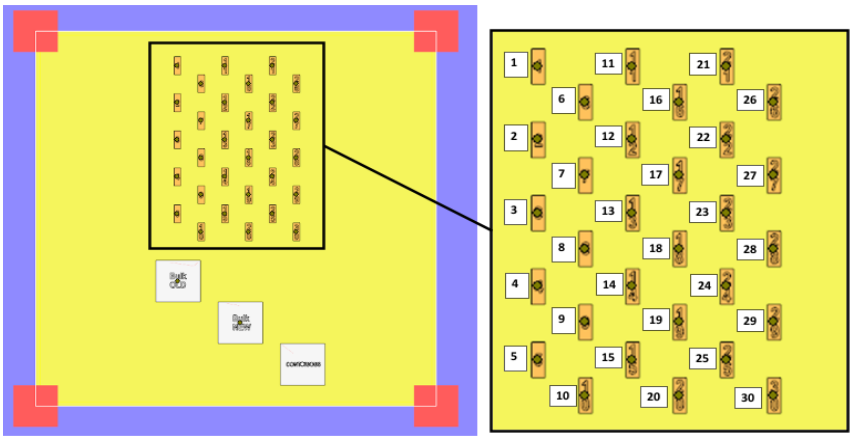

Figure 3.2: Schematic showing manufacture location on build plate with insert showing location for each sample.

Each strain rate includes three samples to verify consistency. These samples' results are averaged to decrease outlier results. To avoid systematic bias due to location on the

build plate, each strain rate includes samples from various sectors of the build plate as shown in Figure 3.3, where SR refers to strain rate.

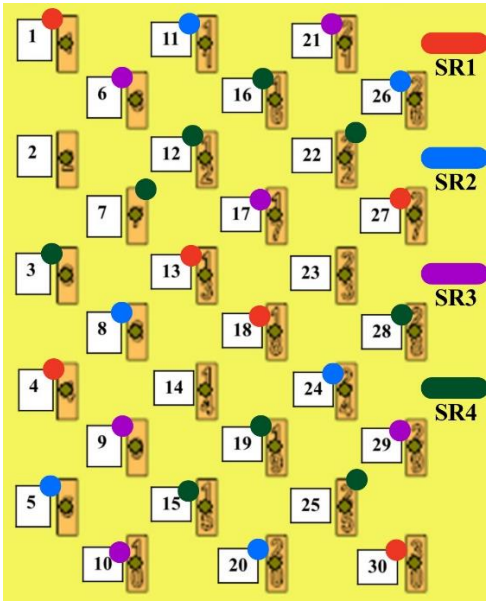

Figure 3.3: Build plate location for samples tested at each strain rate.

3.2 Specimen Preparation

Before each test, the specimens are measured and speckled for digital image correlation (DIC). The DIC is done so that a full field strain measurement can be taken and a virtual extensometer can be used to measure the deformation of the gauge section. Specimens are measured using a micrometer for the thickness and the width. The gauge length is verified to be approximately 7.62 mm using a caliper due to difficulty to achieve measurements as precise as in other directions. The surface is unfinished from after manufacturing.

Table 3.2: Geometric Dimensions and build plate location of each test specimen.

Test Name	Build Plate Location	L (mm)	w (mm)	t (mm)
AM316L-HT-SR1-N1	1	7.62	2.794	1.563
AM316L-HT-SR1-N2	13	7.62	2.871	1.560
AM316L-HT-SR1-N3	4	7.62	2.819	1.561
AM316L-HT-SR2-N1	11	7.62	2.822	1.562
AM316L-HT-SR2-N2	8	7.62	2.819	1.557
AM316L-HT-SR2-N3	5	7.62	2.813	1.563
AM316L-HT-SR3-N1*	2	7.62	2.816	1.565
AM316L-HT-SR3-N2*	14	7.62	2.814	1.558
AM316L-HT-SR3-N3	10	7.62	2.823	1.557
AM316L-HT-SR3-N4	6/9†	7.62	2.821	1.563
AM316L-HT-SR3-N5	6/9†	7.62	2.814	1.563
AM316L-HT-SR4-N1	12	7.62	2.819	1.562
AM316L-HT-SR4-N2	3	7.62	2.827	1.562
AM316L-HT-SR4-N3	15	7.62	2.808	1.560
AM316L-HT-SR4-N4	7	7.62	2.818	1.563
AM316L-AB-SR1-N1	30	7.62	2.804	1.541
AM316L-AB-SR1-N2	18	7.62	2.802	1.549
AM316L-AB-SR1-N3	27	7.62	2.805	1.551
AM316L-AB-SR2-N1	20	7.62	2.793	1.537
AM316L-AB-SR2-N2*	23	7.62	2.805	1.548
AM316L-AB-SR2-N3	26	7.62	2.804	1.557
AM316L-AB-SR2-N4	24	7.62	2.805	1.543
AM316L-AB-SR3-N1	29	7.62	2.808	1.546
AM316L-AB-SR3-N2	17	7.62	2.795	1.553
AM316L-AB-SR3-N3	21	7.62	2.798	1.541
AM316L-AB-SR4-N1	19	7.62	2.795	1.560
AM316L-AB-SR4-N2	28	7.62	2.799	1.546
AM316L-AB-SR4-N3	16	7.62	2.819	1.547
AM316L-AB-SR4-N4	22	7.62	2.802	1.547
AM316L-AB-SR4-N5	25	7.62	2.794	1.542

†: Specimen 6 and 9 are identical after manufacturing, but before testing, each one is labeled as N4 or N5 as writing on the specimen, and they were measured as N4/N5 instead of a 6/9.

*: Test failed and DIC was not captured, and repeat tests were performed at these conditions.

The naming convention describes material, which is additively manufactured 316L stainless steel (AM316L), the heat treatment of the sample in the as-built (AB) or heat-

treated (HT) condition, the target strain rate (SR1: $10^{-3}\ s^{-1}$, SR2: 1000 s^{-1}, SR3: 2500 s^{-1}, SR4: 5000 s^{-1}), and the test number in the series (N1-N5).

Quasi-Static (SR1) Specimens are speckled using a white can of spray paint for the base coat, and the black speckle pattern is done using an Iwata Smart Jet Pro Compressor with an airbrush attachment, as shown in Figure 3.4. The target speckle size is approximately four pixels per paint speckle.

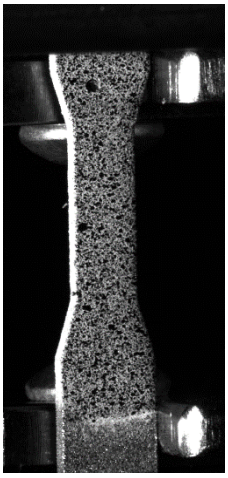

Figure 3.4: Sample Speckle from Quasi-Static Testing (AM316L-AB-SR1-N2 from Left Camera).

The dynamic specimens are also measured prior to speckling, but the speckling procedure is slightly different. Due to the lower resolution of the higher rate camera, the speckle pattern required is bigger to ensure accurate strain data. The larger speckle pattern is created using a white base coat from a white spray paint can, and the speckles are created using a black spray paint can. Large spray pattern is created by holding down the top of the can with less force than required to fully spray the can, such that the can just "sputters." Often, this created a few speckles that were too big, and these were corrected by redoing the speckle completely or by "doctoring" the speckle by dabbing some white paint on the large black spot to shrink it down. Figure 3.5 shows a sample speckle on a dynamic test specimen.

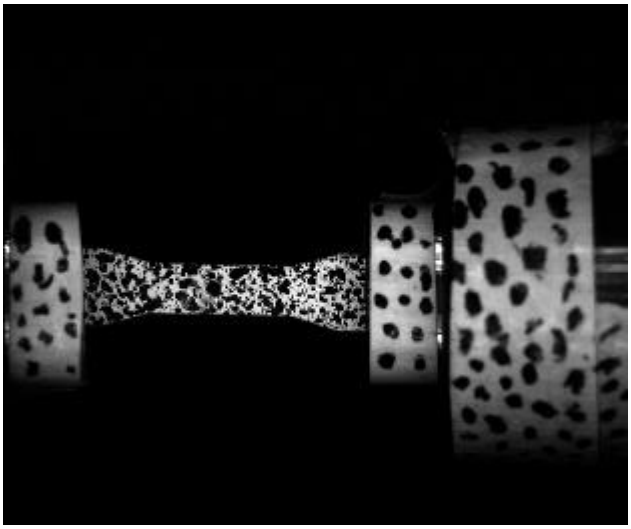

Figure 3.5: Sample speckle pattern from dynamic testing (AM316L-AB-SR4-N1).

Speckled tape is also placed on the split-Hopkinson bar's grips so that the DIC can track the displacement of the transmitter and incident bars of the split-Hopkinson bar. This allows force readings to be verified due to the ability to solve for displacement in the bars using the strain gages and comparing that reading to the DIC displacement. The 3D DIC is utilized on the quasi-static tests using Correlated Solutions' VIC 3D 9, and 2D DIC is utilized on the dynamic split-Hopkinson bar tests using Correlated Solutions' VIC 2D 7.

3.3 Quasi-Static Tension Testing

The quasi-static testing is completed at a target strain rate of $10^{-3}\ s^{-1}$ using an MTS 858 Mini Bionix II. This hydraulic load frame records force and displacement at 100 Hz. The maximum force of the load cell is 25,000 N. An alignment tool is placed inside the grips of the load frame such that the grip of the samples could be pressed against it to ensure straight vertical alignment of the sample. This ensures that the test is in uniaxial tension and no bending is done on the specimen. The specimen is placed inside the hydraulic grips, and the grips are closed at the lowest pressure that will close the grips and hold the

specimen in place. Due to wedge action grips, this creates a small elastic force in the specimen, which is zeroed out by moving the crosshead slightly before the grips are closed to full pressure.

The DIC system used for the quasi-static testing is a 3D DIC system, which requires two cameras at between a 30° and 15° angle between them to ensure the most accuracy ("Calibration Using VIC" 2022). The cameras used are 5MP Basler acA2440-75um cameras, which have a resolution of 2448 x 2048. These cameras' settings are adjusted to ensure the clearest view of the sample, considering that the samples are going to deform. This means more room is required in the direction of the movement of the crosshead.

The crosshead is set to move at a speed of 131 seconds per 1 mm, or 7.62 μm/s because to achieve a strain rate of $10^{-3}\ s^{-1}$, the required velocity is calculated using Equation (3.1):

$$\dot{\epsilon}_e L = v_c\ , \tag{3.1}$$

where $\dot{\epsilon}_e$ is the engineering strain rate, L is the gauge length, and v_c is the crosshead velocity.

The test begins, and the force and displacement are both recorded as a function of time. For the first test (AM316L-HT-SR1-N1), a frame rate of 2 frames per second (fps) is used. At completion, this results in over 3600 pictures, so the frame rate is reduced for the remaining quasi-static tests to a frame rate of 0.2 fps, which results in around 300 frames total for each test (between the two cameras).

3.4 Dynamic Split-Hopkinson Bar Tension Testing

The samples are installed into the tension grips using a hydraulic Enerpac P392 hand pump to secure the samples in the grips. The hydraulic hand pump is used to press the press

the wedge grips into the wedge housing such that the grips clamp harder into the samples up to a hydraulic fluid pressure of 30 MPa or 300 bar. The purpose of using wedge grips is that the grips tighten on the sample as tension is applied, as shown in Figure 3.6. The grips are pressed from the back with the hydraulic hand pump to compress the sample in the grips.

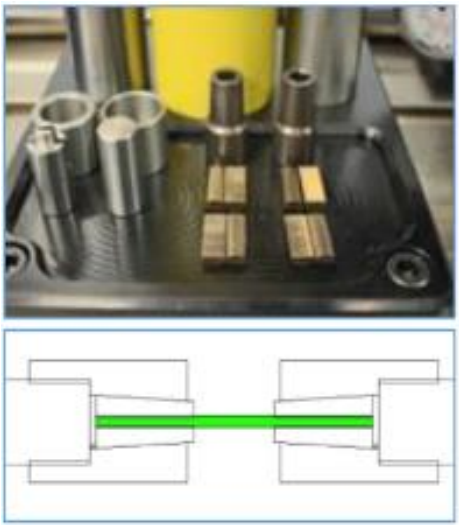

Figure 3.6: SHB dynamic tension test grip setup showing (a) a picture of the physical grips used and (b) a diagram of the wedge grips (Anderson 2020).

The sample and grips are then screwed over the ends of the split-Hopkinson bar to ensure the tension wave is transmitted into the grips before wave reflections can occur in the end of the bar.

The strain gages are controlled using a Micromeasurements 2310 signal conditioner, which supplies an excitation voltage of 15V. The strain gages are then calibrated by adjusting the gain such that $1000\mu\epsilon$ is shown as 2V. This is a function of the signal conditioner to show the calibration voltage. The voltages are zeroed out using a trim knob, which adjusts the baseline voltage, where the signal is run through two LEDs, and when both of them are off, the signal is at 0V. This is because zero strain is represented by 0V.

The voltage out of the strain gages are measured by two oscilloscopes: a Pico Technology 2206B and a Pico Technology 4224. The Pico Technology 2206B oscilloscope is able to trigger the camera using a 5V square wave when tension in the bar is detected, but the Pico Technology 4224 oscilloscope is able to read the strain gages more accurately, so both of them are required. The 2000 Series is used to trigger the camera, and the strain gauge is recorded for analysis is using the 4000 series.

When the oscilloscope detects a tension wave, it sends a 5V trigger signal to the camera, a Shimadzu HPV-2. The camera receives the signal, waits a set delay, and begins recording at a set frame rate, exposure, focus, focal length, aperture, and other manually set presets. Because the camera receives a trigger signal when the tension wave reaches the strain gage, which is 91 cm from the sample, a delay to allow the tension wave to reach the sample is added to the camera. In this setup, a delay of 160 μs is added to each test, and this ensures that 20-30 μs of images before and after the test are captured over a total of 102 frames stored per trigger. Because the high-rate tests are recorded at 500,000 fps, 102 frames capture 202 μs of testing.

The REL split-Hopkinson Pressure Bar is used to perform the dynamic strain rate tests. The bar used is a 1.9 cm diameter C350 Maraging Steel bar with a 244 cm transmitter bar, a 198 cm transmitter bar, and a 30.5 cm long striker bar. The Young's Modulus, E, of the all three bars is 196.2 GPa, the density, ρ, is 7999.5 $\frac{kg}{m^3}$, and the wave speed in the bar is 4952 m/s as calculated by Equation (2.7).

The following are the results from quasi-static and dynamic tension tests of L-PBF 316L stainless steel. All strain rates are reported as engineering strain rates.

Chapter 4. Results

4.1 Quasi-Static Tension Testing Results

The quasi-static strain results are calculated using a virtual extensometer on a 3D DIC system, and force results are recorded using the hydraulic load frame's load transducer. Three tests of heat-treated and as-built are each completed to ensure consistency. The samples are all gripped on a similar place on the grip section of the sample.

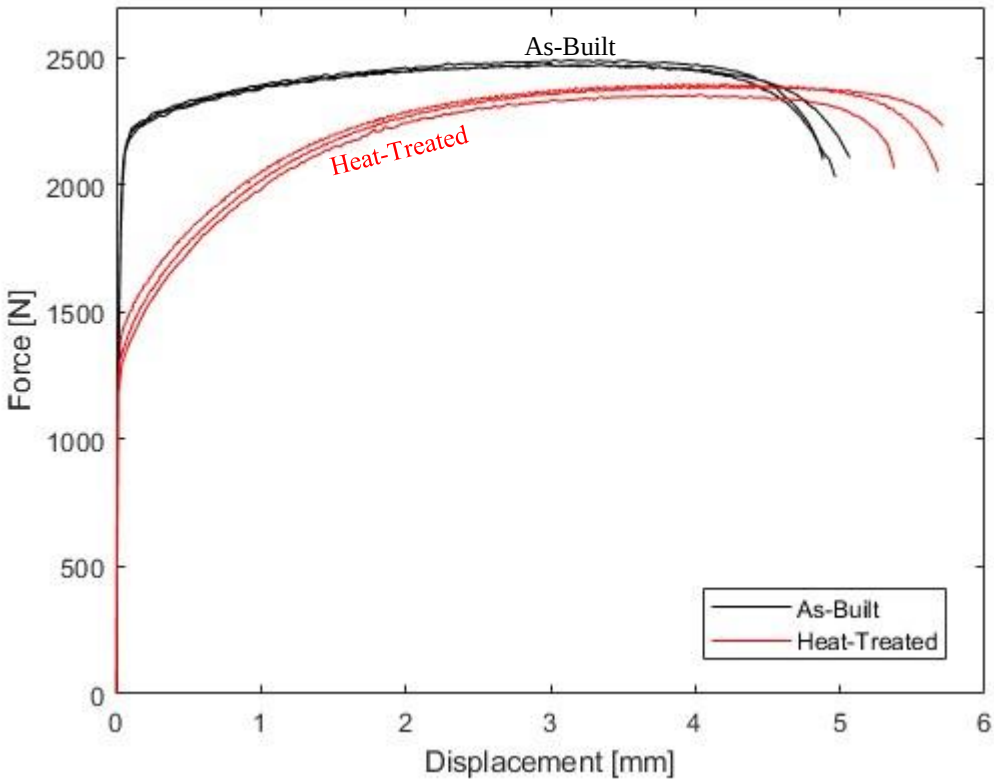

Figure 4.1: Quasi-Static force vs. displacement curves on AB and HT 316L AM steel.

Since the tests are consistent as shown by Figure 4.1, the data is analyzed and stress vs. strain curves are created from the measured force and extensometer displacement converted to true stress and true strain using Equations (2.3) and (2.4) using the measured dimensions and a gauge length of 7.62 mm in Figure 4.2. The target strain rate is $10^{-3}\ s^{-1}$, but due to the grip section of the sample being strained to some extent, the actual strain rate was slightly decreased from the target, achieving in reality $6 \times 10^{-4}\ s^{-1}$ to $8 \times 10^{-4}\ s^{-1}$.

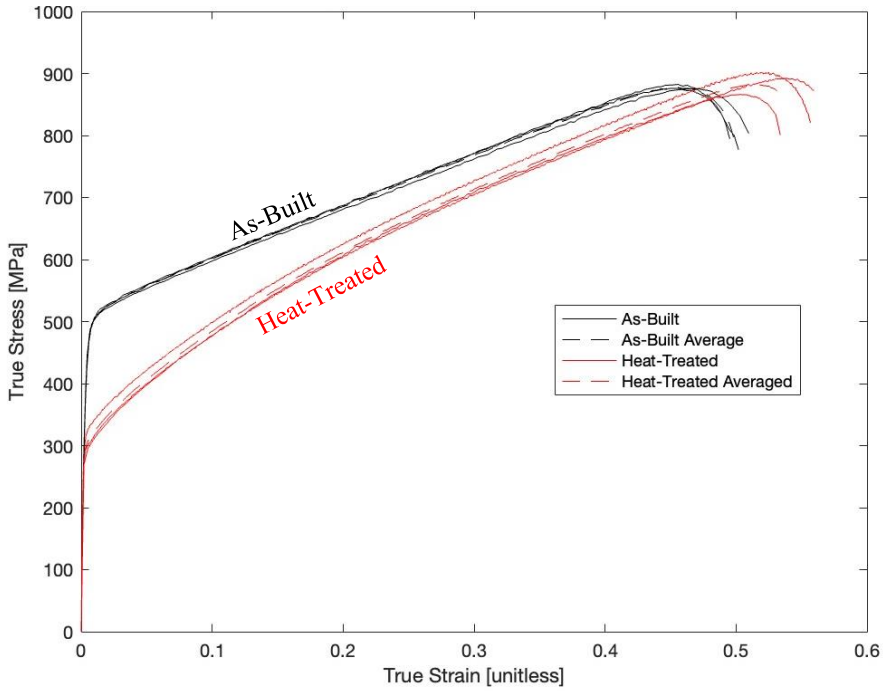

Figure 4.2: Extensometer stress vs. strain curves at quasi-static strain rate ($6 \times 10^{-4}\ s^{-1}$ for HT & $8 \times 10^{-4}\ s^{-1}$ for AB).

The quasi-static stress vs. strain curves show a linear elastic region, but due to lack of data in the elastic region, an elastic modulus of 193 GPa is found using MATWEB for both as-built and heat-treated for yield stress calculation purposes ("AISI Type 316L"). An average yield stress of 422 MPa is found using the 0.2% offset method in accordance with ASTM E8 for the as-built, and an average yield stress of 297.3 MPa is found for the heat-treated samples, also using the 0.2% offset method. The as-built samples' plastic region is

close to linear hardening rate until necking, where the samples fracture at 0.495 - 0.510 true strain. The heat-treated samples display nonlinear hardening in the plastic region, where they yield at a much lower stress than the as-built, but they strain harden quicker and fracture at roughly the same stress. They fracture at a slightly higher true strain value of 0.534 - 0.560.

These curves from each test are averaged and the different heat treatments are compared. The stress vs. train curves made using the Hencky strain are also averaged from each test and plotted against the extensometer strain in Figure 4.3.

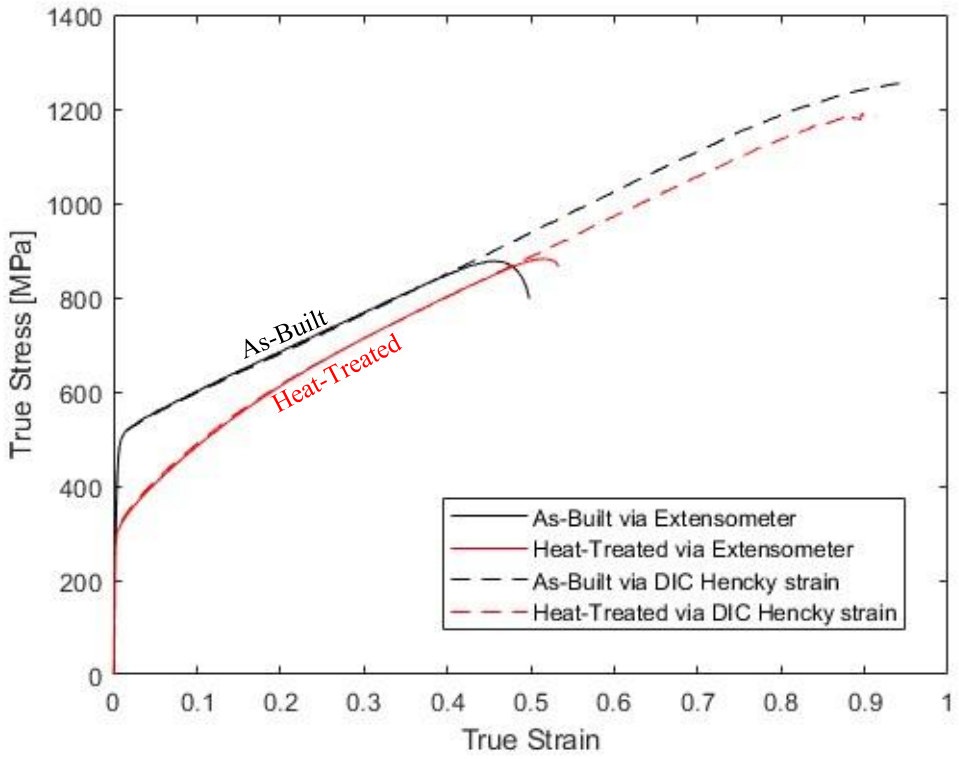

Figure 4.3: Averaged comparison of true stress vs. true strain curves found using extensometer conversion and local DIC Hencky strain.

4.2 Dynamic Tension Testing Results

The dynamic results are completed using a split-Hopkinson bar. From firing blank shots at various pressures, the following correlation between the tank pressure and the striker velocity was found using Equation (4.1):

$$P = 0.7645V^2 + 0.7624V + 74.9605\,, \tag{4.1}$$

where V is the target velocity in m/s, and P is the pressure used in kPa.

Due to the striker bar length being 30.5 cm, and the theoretical pulse length being twice the time it takes for the wave to travel from one end of the striker bar to the other, the theorical pulse length is 123 μs. This is calculated using Equation (4.2):

$$t = \frac{2L}{c_b}\,, \tag{4.2}$$

where t is the pulse length, L is the striker bar length, and c_b is the wave speed in the bar.

Loading only occurs for the duration of the pulse. Due to the ductility of the samples, fracture did not occur within one loading pulse for most tests.

Images are taken of the dynamic tests at 500,000 fps. The delay is the amount of time between when the strain gauge detects a wave and when the camera turns on. The delay is set to 160 μs to allow the wave to get from the gage to the sample. Calibration images are taken for DIC analysis by taking a picture of a ruler using the camera to ensure an accurate mm/pixel measurement.

4.2.1 2nd Strain Rate (1000 s^{-1})

The target strain rate is 1000 s^{-1}, but like the quasi-static results, the actual strain rates differed somewhat, achieving 700 s^{-1} – 800 s^{-1} in the HT samples with one outlier at 600 s^{-1}, and 800 s^{-1} – 900 s^{-1} in the AB in average engineering strain rate. The

following stress vs. strain curves were achieved using a 131 kPa shot and an actual velocity of the striker bar of 8 m/s to 9 m/s, and one outlier of 7 m/s resulting in the lower strain rate reported above in the HT results. The pressure in the pressure vessel was achieved with an air compressor using ambient air. The wave data from the as-built and heat-treated results is shown below in Figure 4.4 and Figure 4.5, respectively.

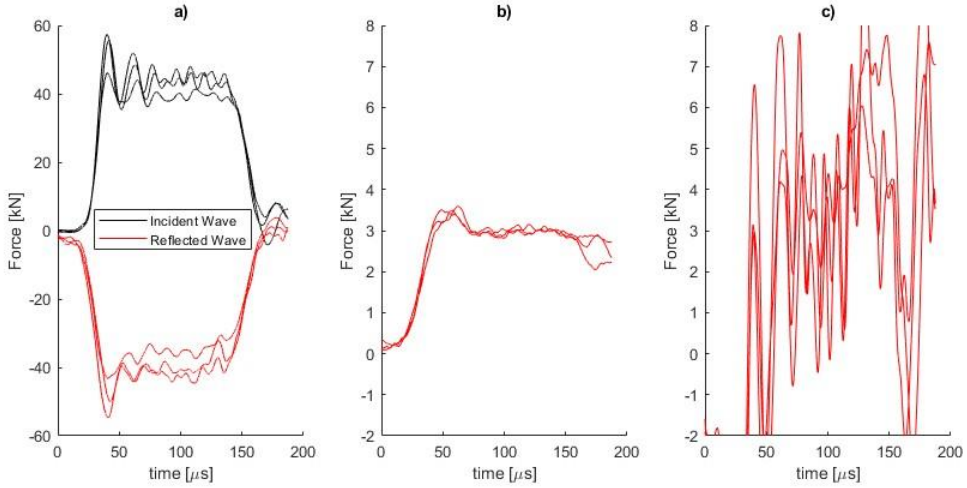

Figure 4.4: Force data constructed from elastic wave analysis from AB samples at SR2, showing (a) waves in incident bar, (b) waves in transmitter bar, and (c) incident added to reflected wave.

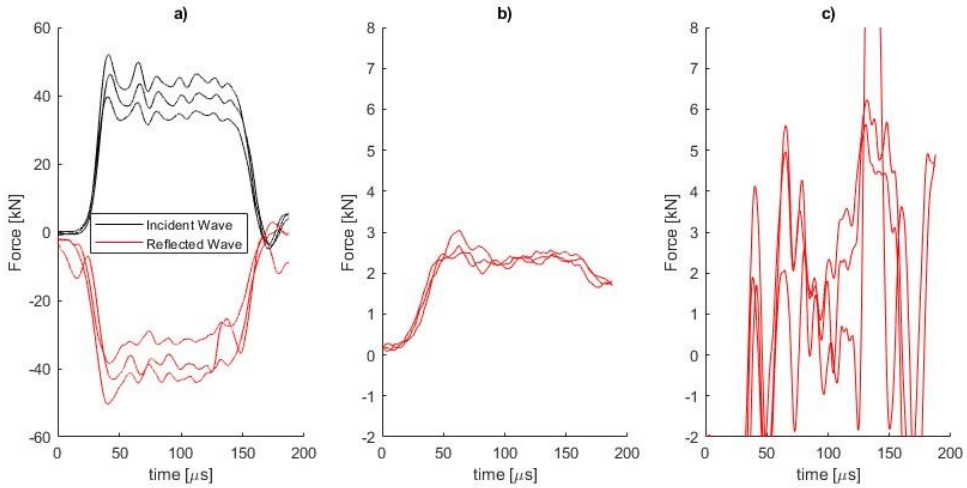

Figure 4.5: Force data constructed from elastic wave analysis from HT samples at SR2, showing (a) waves in incident bar, (b) waves in transmitter bar, and (c) incident added to reflected wave.

The above Figure 4.4 (c) and Figure 4.5 (c) show the two-wave analysis conducted in the SR2 results. The high oscillations in the incident wave makes the force on the incident bar also have lots of oscillations, making verification of force equilibrium difficult. However, the data shows that the force on incident side of the sample is in the same order of magnitude as the transmitter side of the sample. Due to higher repeatability and lower oscillations in the transmitter bar, stress vs. strain curves are constructed using a 1-wave analysis on the transmitted wave, as shown in Figure 4.6.

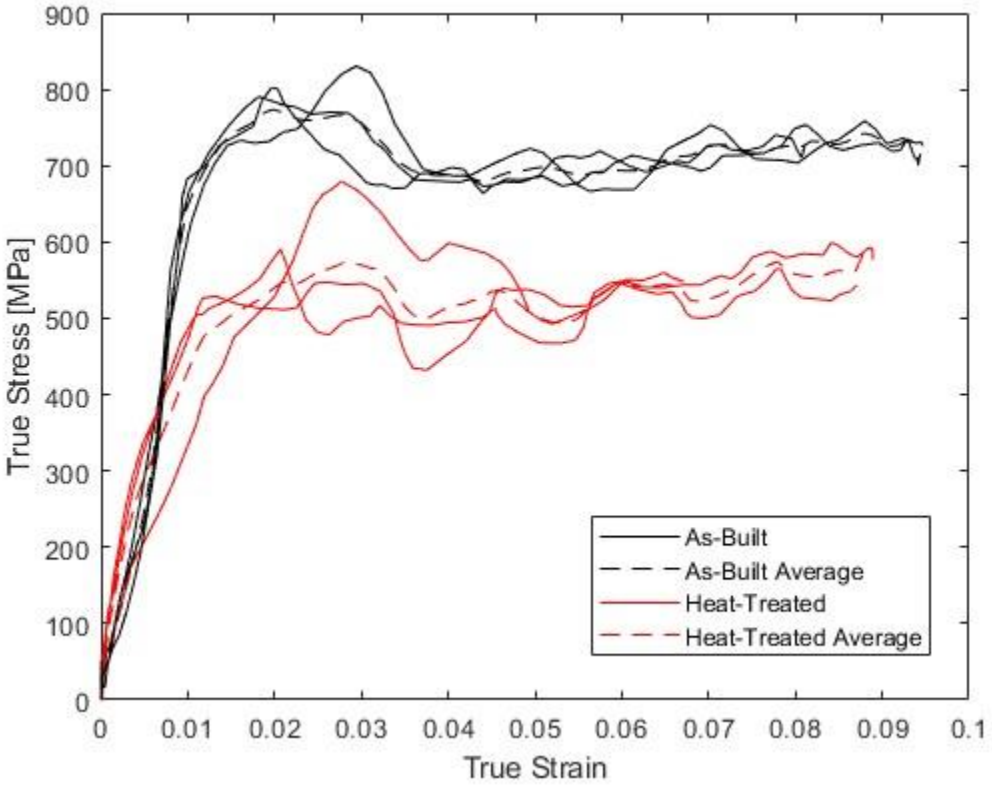

Figure 4.6: Results from SR2 (600 s^{-1} - 800 s^{-1} in HT and 800 s^{-1} - 900 s^{-1} in AB) with average curves.

The results from Figure 4.6 show a higher flow stress in the as-built configuration. There is little strain hardening, but the strain levels are low relative to the expected failure strain (~50%). None of the samples fractured at this strain rate.

4.2.2 3rd Strain Rate (2500 s^{-1})

Due to undershooting the previous strain rates, the pressure is increased to 689 kPa to more accurately achieve the target strain rate. After the scaling, the actual achieved strain rate was 2500 s^{-1}-2600 s^{-1} for the heat-treated samples, and 2900 s^{-1} for the as-built samples. The tests were completed using a 689 kPa shot for each test and an actual striker bar velocity 26 m/s to 27 m/s. The pressure was achieved using an air compressor using ambient air. The wave data from SR3 is shown below in Figure 4.7 and Figure 4.8.

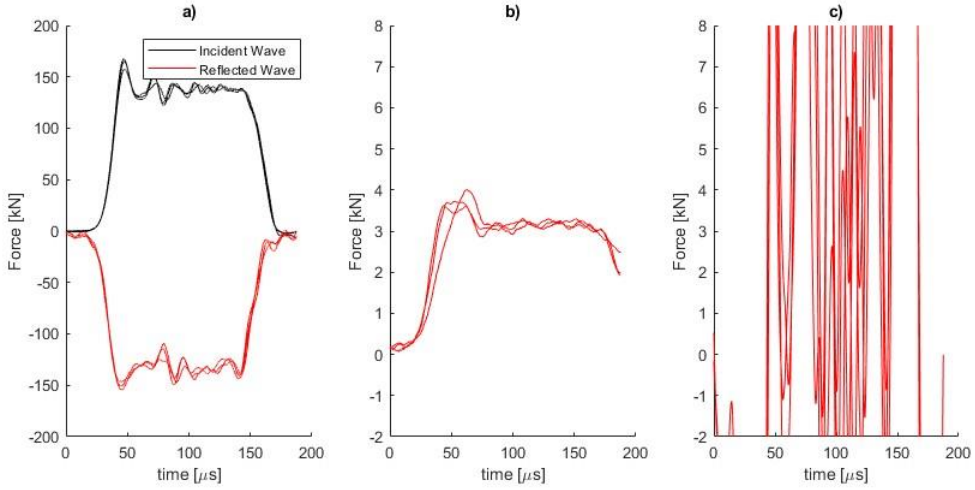

Figure 4.7: Force data constructed from elastic wave analysis from AB samples at SR3, showing (a) waves in incident bar, (b) waves in transmitter bar, and (c) incident added to reflected wave.

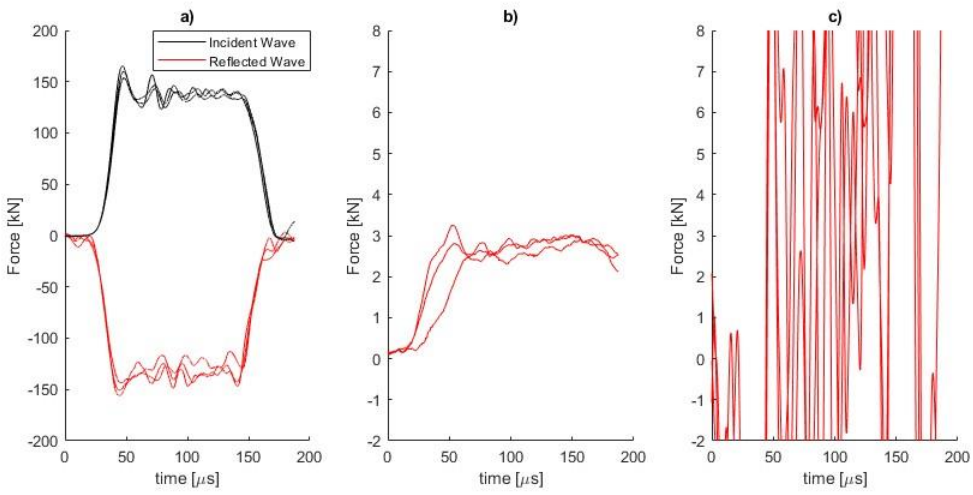

Figure 4.8: Force data constructed from elastic wave analysis from HT samples at SR3, showing (a) waves in incident bar, (b) waves in transmitter bar, and (c) incident added to reflected wave.

Due to the amplified oscillations in SR3 when compared to SR2, a 1-wave analysis was again used to create stress vs. strain curves at SR3 as shown in Figure 4.9.

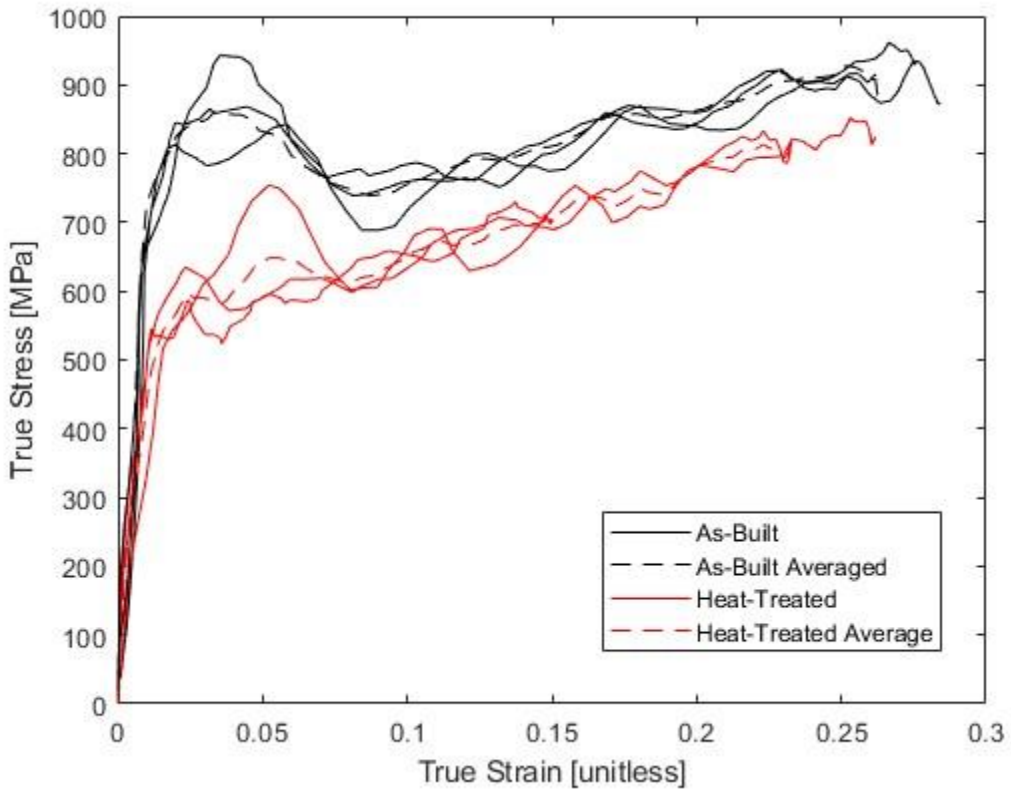

Figure 4.9: Results from SR3 (2500 s^{-1} in HT and 2900 s^{-1} in AB) with average curves.

The discrepancy between the as-built and heat-treated results was more apparent at SR3 than in previous tests. The as-built samples exhibited a higher strain rate than the heat-treated for the same velocity impact. This is contrary to what was expected. Since the as-built samples have a higher flow stress, it was expected that the as-built would resist deformation more and exhibit a lower strain rate. The as-built recorded a 2908 s^{-1} to 2947 s^{-1} strain rate whereas the heat-treated samples recorded 2539 s^{-1}-2548 s^{-1} with one outlier at 1217 s^{-1} due to the grips not being properly seated. Where generally other tests showed a plateau in strain rate, the outlier showed a steady increase in strain rate where the grips had not caught the sample, finishing at 2500 s^{-1} with the other results.

The SR3 results showed significantly more strain hardening than in SR2 and a further increased yield stress. HT and AB both show inertial effects until 5% to 10% strain where the yield stress appears higher than it actually is. However, this effect is due to resistance to motion and acceleration due to the mass and inertia in the material and not an actual indicator of the mechanical response of the material. Both HT and AB showed a fairly linear hardening rate past the early peak due to inertial effects in the material.

4.2.3 4th Strain Rate (5000 s^{-1})

The fourth strain rate is a target strain rate of 5000 s^{-1}. Due to inconsistencies between recorded strain rates at the same firing velocities for each heat treatment, a higher velocity was used on the heat-treated samples than the as-built to ensure consistency in results. Due to the air compressor not being able to compress to the needed pressure, compressed nitrogen is used in the pressure vessel. This also ensures homogeneity in the expanding gas that fires the striker bar, which will cause more consistency in the striker bar velocity. For

the as-built samples, the vessel was pressurized to 1590 kPa, and the heat-treated tests were pressurized to 1720 kPa. The limit of the vessel is 2070 kPa, so these pressures are within the limits for safety. The resulting velocities were 41 m/s for the as-built samples and 42 m/s to 43 m/s for the heat-treated samples. The wave data from SR4 is shown below in Figure 4.10 and Figure 4.11.

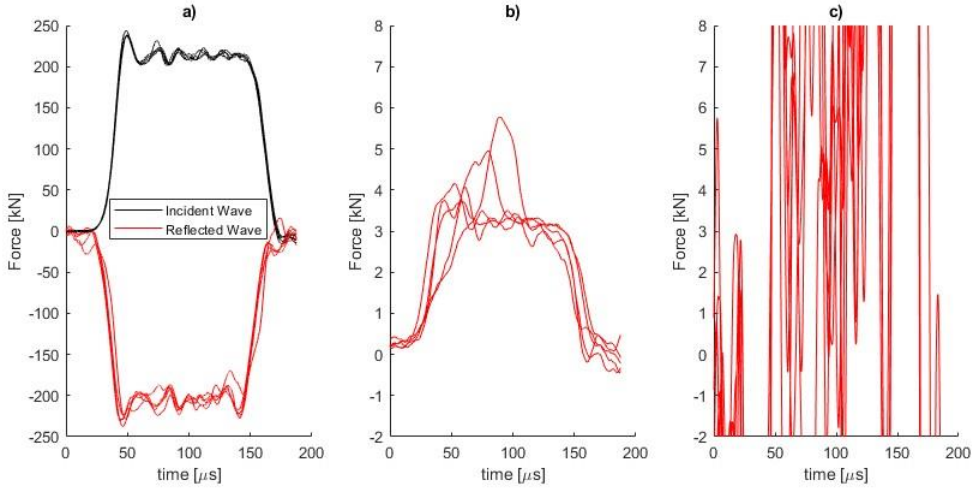

Figure 4.10: Force data constructed from elastic wave analysis from AB samples at SR4, showing (a) waves in incident bar, (b) waves in transmitter bar, and (c) incident added to reflected wave.

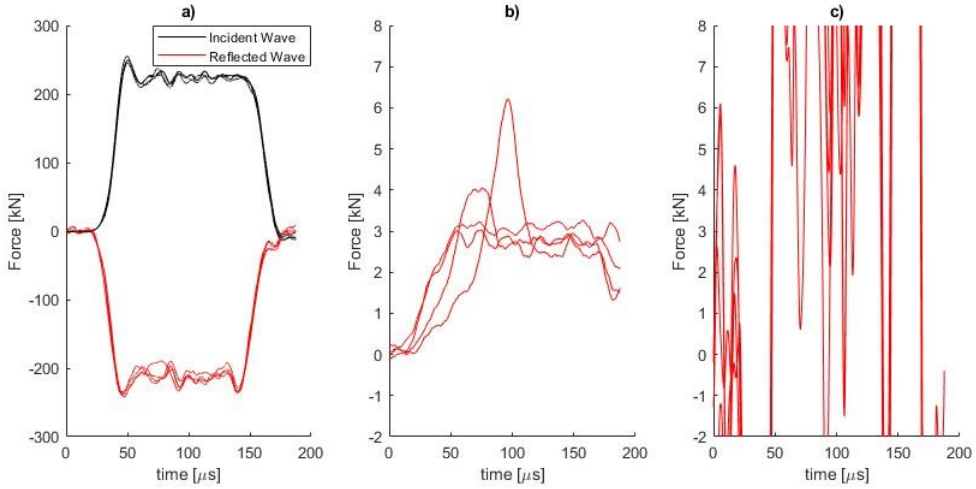

Figure 4.11: Force data constructed from elastic wave analysis from HT samples at SR4, showing (a) waves in incident bar, (b) waves in transmitter bar, and (c) incident added to reflected wave.

High peaks in the data occurred in some of the transmitted waves of the samples. It is probable that these high peaks are not material properties, but due to inertial effects and wave reflections at the grips. A 1-wave analysis was also conducted for the SR4 results as shown in Figure 4.12 below.

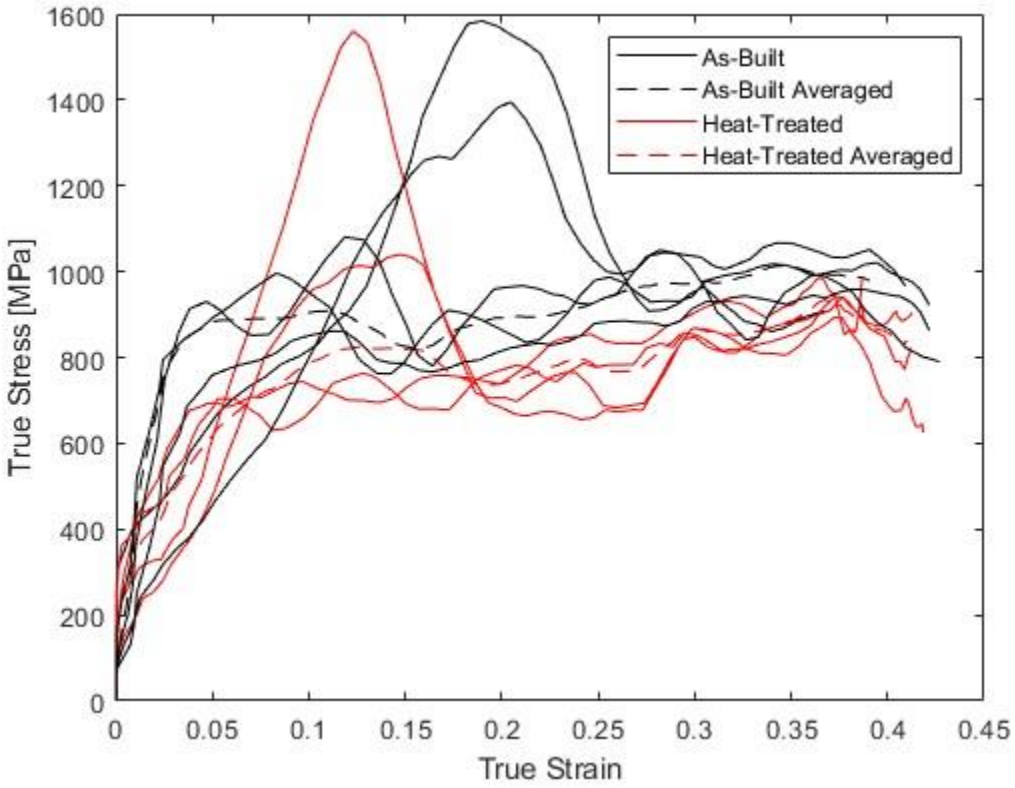

Figure 4.12: Results from SR4 (4300 s^{-1} - 4400 s^{-1} in HT & 4700 s^{-1} - 4800 s^{-1} in AB) with average curves.

In this case, the as-built samples all fracture, but none of the heat-treated samples do. It is unclear how the dynamic tests affect the fracture strain for the heat-treated samples. As can be seen, there are two results from the as-built group and one result from the heat-treated group that display major peaks in stress level at around 10% - 20% strain. It is probably not a material property and more of an effect of the test setup. The increased stress

levels could be cause by increased oscillations in the incident wave, wave reflections at the specimen-grip interface, or other effects of the high velocity shot that made repeatable results more difficult to obtain. Due to the repeatability of the remaining force measurements without peaks, the transmitted waves with the high oscillations were treated as outliers and omitted from the average curve, which means that three curves are included in each average curve at this strain rate.

4.3 Combined Results

The combined results show the strain rate sensitivity of the samples in each heat treatment condition in Figure 4.13 below by showing the average curve at each strain rate.

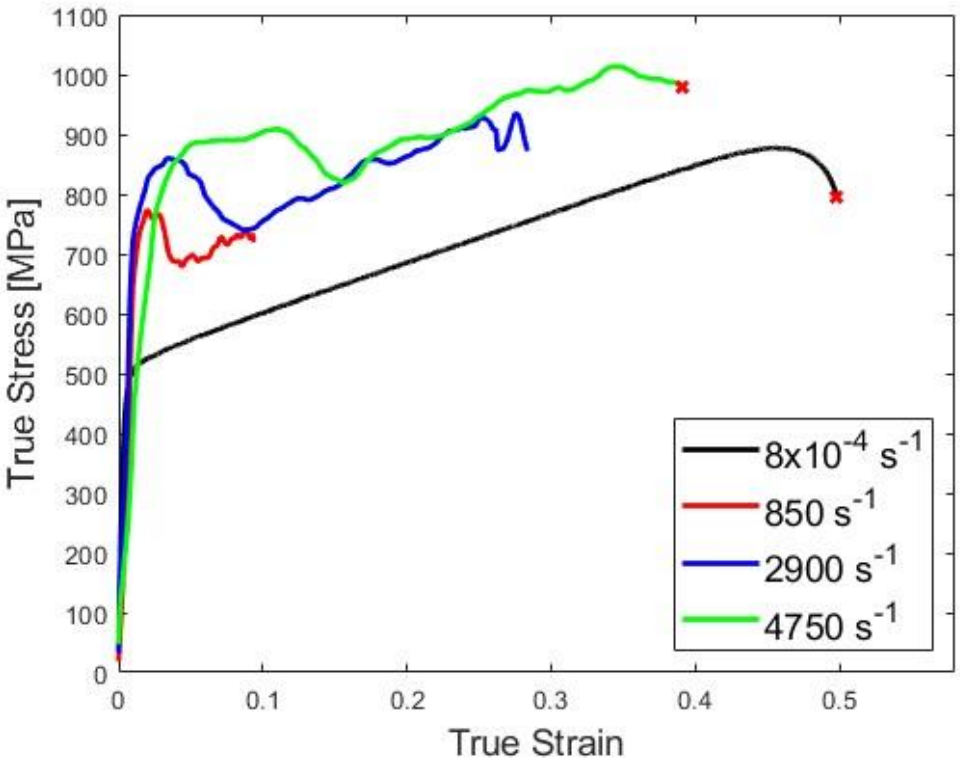

Figure 4.13: As-built average stress vs. strain curves at all strain rates. The red "x" indicates which tests fractured.

At 4750 s^{-1}, the as-built samples fracture and demonstrate a decrease in fracture strain from the quasi-static results. The average fracture strain of the quasi-static as-built results is 50.23% strain, and the average fracture strain at 4750 s^{-1} is 40.74% strain, for a 19% decrease in overall fracture strain. The as-built samples show a strain rate sensitivity between the quasi-static testing and the dynamic, but very little sensitivity over just the dynamic results. One possible reason this could be is that there is a much larger jump in strain rate from the quasi-static ($8 \times 10^{-4}\ s^{-1}$) to SR2 (850 s^{-1})—6 orders of magnitude—as compared to the rest of the strain rates only increasing about a half an order of magnitude from SR2 (850 s^{-1}) to SR4 (4750 s^{-1}). Another potential reason for the stress vs. strain curves aligning to have the same flow stress level is that due to the high ductility of the sample, the true strain rate decreases significantly as the test goes on due to Equation (2.5). This means that as the 4750 s^{-1} tests continue, the true strain rate when the new, elongated sample length is considered is considerably lower. However, the true strain rate is still relatively high throughout the test. This effect of the specimen ductility on the true strain rate can be seen in Figure 4.14.

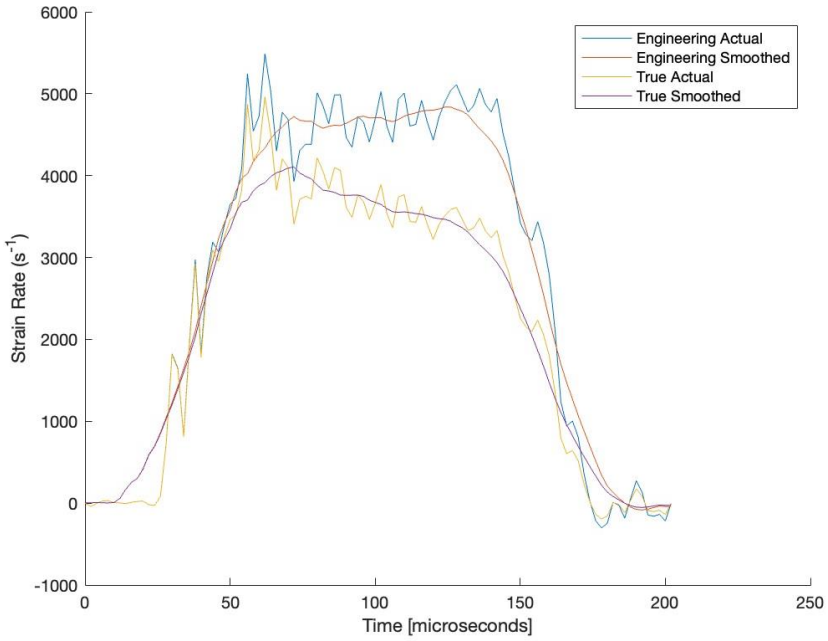

Figure 4.14: Strain rate plot AM316L-AB-SR4-N3, comparing engineering and true strain rates.

As the test continues, the engineering strain rate stays near 5000 s^{-1} but the true strain rate drastically decreases to around 3000 s^{-1}, potentially a reason that the dynamic stress vs. strain curves join up at the later strain values. Because the true strain uses the instantaneous strain in the sample to be calculated, samples that fracture at a lower strain value do not exhibit this phenomenon to this extent. As the sample material is relatively ductile, the decrease in true strain rate is exacerbated and would not be as apparent on samples with lower ductility. Since split-Hopkinson bars move the incident bar at a relatively constant velocity, this phenomenon cannot be avoided with the current test setup.

However, the heat-treated samples exhibit increased flow stress levels with increases in strain rate, as shown in Figure 4.15.

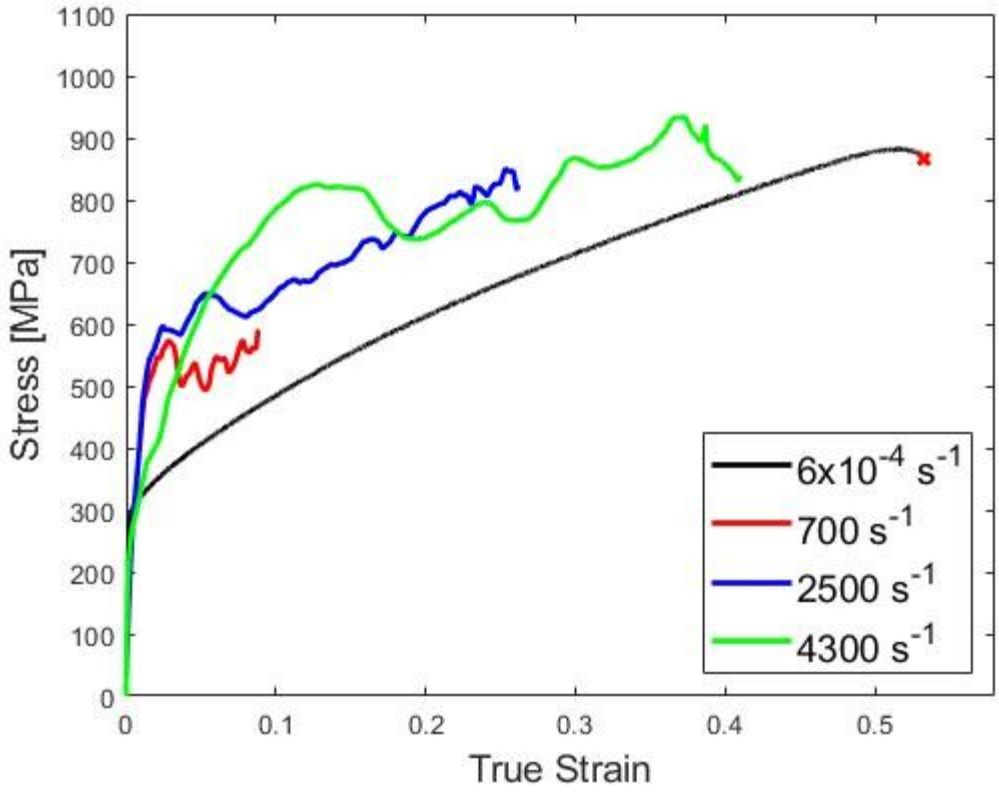

Figure 4.15: Heat-treated average stress vs. strain curves at all strain rates. The red "x" indicates which tests fractured.

The low repeatability of the 4300 s^{-1} strain rates tests is apparent, as there is high variability and oscillations in the results. However, strain rate sensitivity is much more apparent between the 700 s^{-1} and 2500 s^{-1} in the heat-treated condition compared to the as-built material. As none of the heat-treated samples fracture, no inferences about the fracture strain can be made.

As each test had a slightly different strain rate, it is reported in Table 4.1 below to show the variability and repeatability for each test.

Table 4.1: Sample target and actual strain rates.

Test Name	Test Apparatus	Target Strain Rate (s^{-1})	Actual Strain Rate (s^{-1})
AM316L-HT-SR1-N1	Load Frame	1×10^{-3}	0.620×10^{-3}
AM316L-HT-SR1-N2	Load Frame	1×10^{-3}	0.609×10^{-3}
AM316L-HT-SR1-N3	Load Frame	1×10^{-3}	0.603×10^{-3}
AM316L-HT-SR2-N1	SHB	1000	722.8
AM316L-HT-SR2-N2	SHB	1000	793.1
AM316L-HT-SR2-N3	SHB	1000	596.1
AM316L-HT-SR3-N3	SHB	2500	1216.5
AM316L-HT-SR3-N4	SHB	2500	2548.0
AM316L-HT-SR3-N5	SHB	2500	2539.1
AM316L-HT-SR4-N1	SHB	5000	4254.7
AM316L-HT-SR4-N2	SHB	5000	4284.7
AM316L-HT-SR4-N3	SHB	5000	4421.6
AM316L-HT-SR4-N4	SHB	5000	4298.9
AM316L-AB-SR1-N1	Load Frame	1×10^{-3}	0.776×10^{-3}
AM316L-AB-SR1-N2	Load Frame	1×10^{-3}	0.784×10^{-3}
AM316L-AB-SR1-N3	Load Frame	1×10^{-3}	0.791×10^{-3}
AM316L-AB-SR2-N1	SHB	1000	775.8
AM316L-AB-SR2-N3	SHB	1000	923.2
AM316L-AB-SR2-N4	SHB	1000	875.3
AM316L-AB-SR3-N1	SHB	2500	2931.9
AM316L-AB-SR3-N2	SHB	2500	2947.5
AM316L-AB-SR3-N3	SHB	2500	2907.7
AM316L-AB-SR4-N1	SHB	5000	4686.3
AM316L-AB-SR4-N2	SHB	5000	4788.5
AM316L-AB-SR4-N3	SHB	5000	4739.6
AM316L-AB-SR4-N4	SHB	5000	4798
AM316L-AB-SR4-N5	SHB	5000	4785.6

4.4 Johnson-Cook Modeling

To quantify the strain rate sensitivity, a Johnson-Cook model is created for each of the as-built and heat-treated conditions according to previously presented Equation (2.14), $\sigma = [\mathrm{A} + \mathrm{B}(\epsilon^{\mathrm{p}})^{\mathrm{n}}]\left[1 + \mathrm{C}\ln\left(\frac{\dot{\epsilon}}{\dot{\epsilon}_{\mathrm{o}}}\right)\right]\left[1 - \left(\frac{\mathrm{T}-\mathrm{T}_{\mathrm{r}}}{\mathrm{T}_{\mathrm{m}}-\mathrm{T}_{\mathrm{r}}}\right)^{\mathrm{m}}\right]$.

However, since temperature sensitivity is not being quantified, a modified version to exclude the temperature sensitivity is fitted using Equation (4.3):

$$\sigma = [A + B(\epsilon^p)^n]\left[1 + Cln\left(\frac{\dot{\epsilon}}{\dot{\epsilon}_o}\right)\right], \tag{4.3}$$

where A is the yield stress, B is the hardening modulus, C is the JC strain rate sensitivity coefficient, and n is the hardening coefficient (Umbrello *et al.* 2007).

A Johnson Cook model is constructed using the quasi-static results in both the AB and HT to find A, B, and n. Stress at different strain rates at a strain value of 8.7% is used for finding the strain rate sensitivity parameter, C, in both AB and HT results because 8.7% is the highest strain value recorded in the heat-treated results at 700 s^{-1}. The strain value of 8.7% is also used for the AB data to ensure consistency. Noise, oscillations, and inertial effects in the SR4 data in both the AB and HT conditions at 8.7% strain causes the data not to be useful in a JC model due to the stress values not being a mechanical response in the material, so the SR4 data in both AB and HT are omitted from the JC model. The results of the Johnson-Cook model for the as-built samples are shown in Figure 4.16.

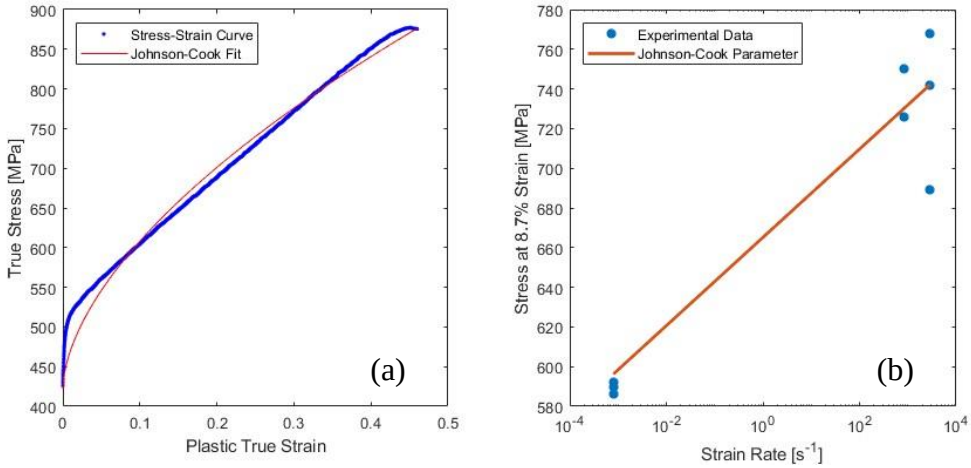

Figure 4.16: Johnson-Cook Model of as-built AM316L SS using extensometer strain: (a) Power law hardening at reference strain rate and (b) Strain rate sensitivity of stress at 8.7% strain.

The as-built model shows that the plastic region of the stress vs. strain curve found does not fit a power law hardening as well as the heat-treated data in Figure 4.17 due to a more linear fit curve, so it does not fit a power law hardening as well, but overall is representative of the curve found.

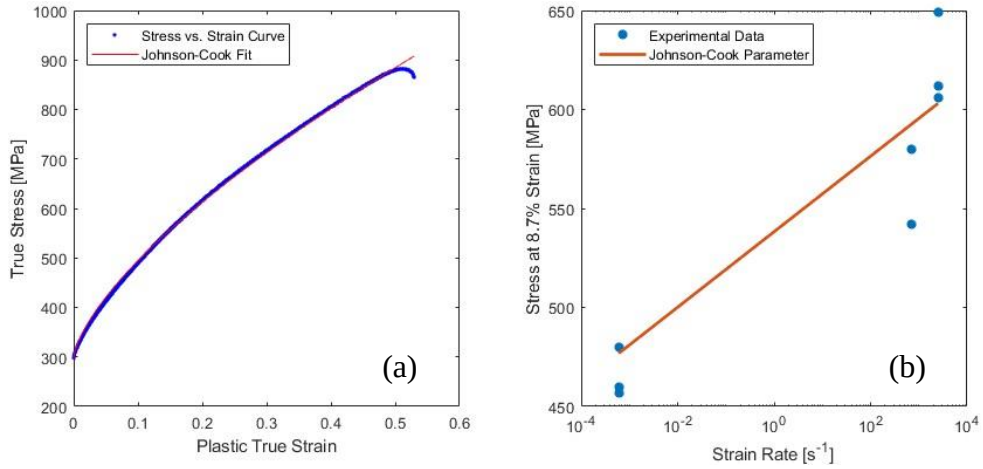

Figure 4.17: Johnson-Cook Model of heat-treated AM316L SS using extensometer strain: (a) Power law hardening at reference strain rate and (b) Strain rate sensitivity of stress at 8.7% strain.

The power law hardening term lines up with the data very well through the entire plastic region due to a curved shape more similar to a power law curve except for the necking region due to the power law's inability to decrease. The heat-treated tests showed a similar strain rate sensitivity to the as-built modelling as shown in Figure 4.16 (b) and Figure 4.17 (b).

Johnson-Cook modelling was not only constructed on the extensometer stress vs. strain curves but also on the DIC Hencky stress vs. strain curves to compare the

(a) (b)

calculated parameters in. Results are shown in Figure 4.18 and Figure 4.19.

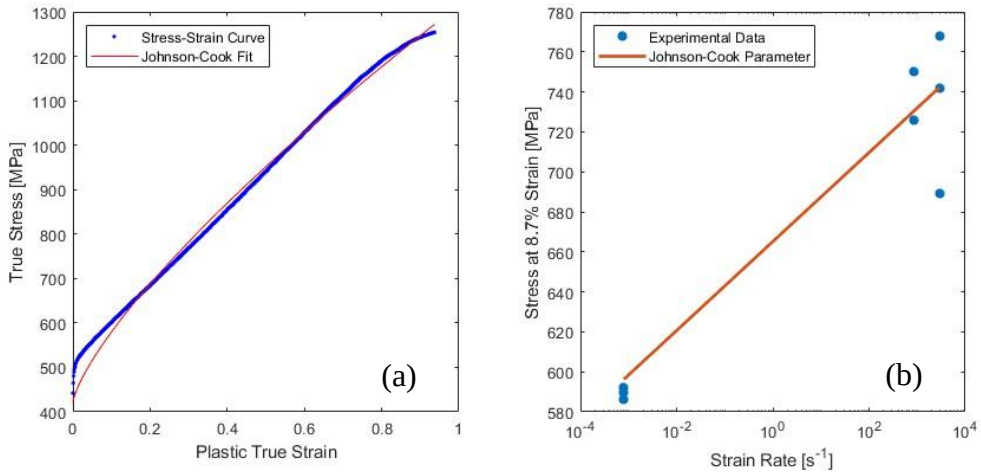

Figure 4.18: Johnson-Cook Model of as-built AM316L SS using DIC Hencky strain: (a) Power law hardening at reference strain rate and (b) Strain rate sensitivity of stress at 8.7% strain.

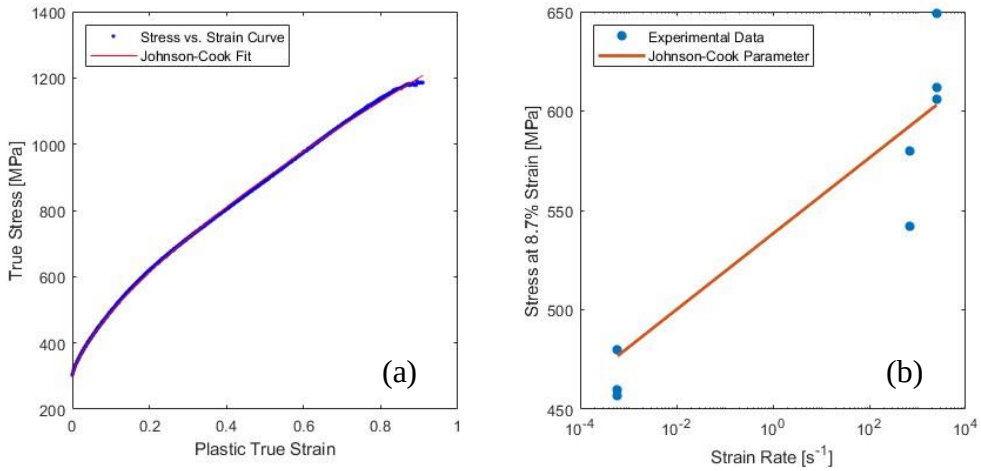

Figure 4.19: Johnson-Cook Model of heat-treated AM316L SS using DIC Hencky strain: (a) Power law hardening at reference strain rate and (b) Strain rate sensitivity of stress at 8.7% strain.

Results from all four Johnson-Cook models are shown in Table 4.2.

Table 4.2: Fitted Johnson-Cook parameters to extensometer and DIC Hencky stress vs. strain curves.

Johnson-Cook Parameters	AB – Extensometer	AB – DIC Hencky	HT – Extensometer	HT – DIC Hencky
A [MPa]	422	422	297.3	297.3
B [MPa]	715.7	892.5	939.3	972.4
n	.5851	.7531	.6778	.6987
C	.0163	.0163	.0174	.0174
$\dot{\epsilon}_0$ $[s^{-1}]$	6×10^{-4}	6×10^{-4}	8×10^{-4}	8×10^{-4}

Because A is the yield stress of the material, A was manually set to be the yield stress, and all other values were found such that the Johnson-Cook model curve at the reference strain rate fits the stress vs. stress curve at the reference strain rate the best by the least squares method. B, the hardening modulus, varied slightly between the true extensometer stress vs. strain curve and the DIC Hencky stress vs. strain curve, varying more in the AB condition than in the HT. The as-built tests showed a slightly lower strain rate sensitivity parameter, C, of 0.0163 than the heat-treated value of 0.0174 for C, but due to the variability of results at higher strain rates, some difference is expected.

Previously documented values by Güden *et al.* (2022) gave a C value of between 0.013 to 0.018 for L-PBF AM316L, which is in the range of the currently determined values. Umbrello *et al.* (2007) also published a list of previously calculated values for the JC parameters for 316L stainless steel, and each value is consistent with their findings.

4.5 Finite Element Simulations

4.5.1 Proportionality Limit as Material Model Yield Stress

The finite element simulations are completed using ANSYS LS-DYNA. The general process for creating a finite element simulation for testing a material model is to create the sample geometry in a CAD software, import the geometry into LS-DYNA, create elements and nodes from the geometry, create a material model, do a simulated tension test on the sample, and compare the simulation results to experimentally observed behavior. Below is a sample of a FEA simulation of a dogbone tension specimen in Figure 4.20.

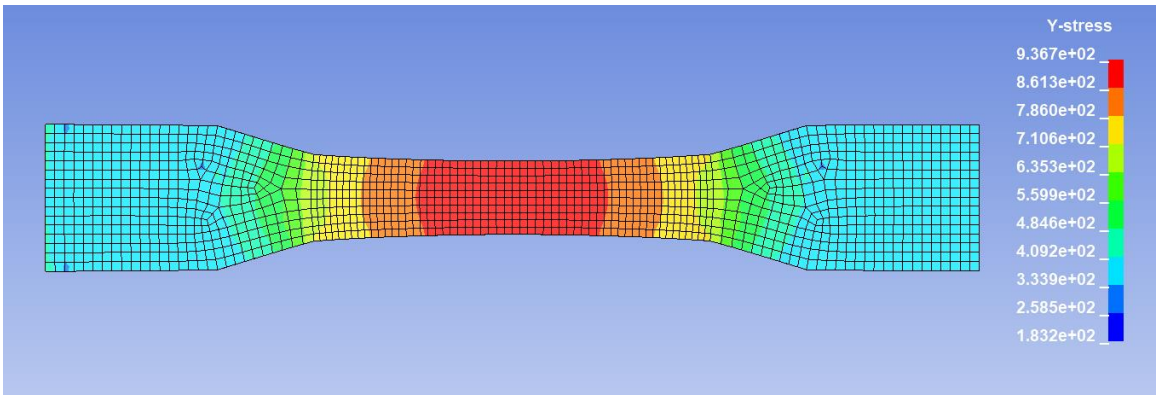

Figure 4.20: Dogbone simulation sample image.

The material model chosen is MAT_PIECEWISE_LINEAR_PLASTICITY or MAT-24 in LS-DYNA (LS-DYNA, 2021). This material model allows the user to define values for E, ν, failure strain, σ_y, and to input a tabulated true stress vs. plastic true strain curve to model the post-yield plastic behavior.

The true stress vs. plastic true strain curve is created by taking the local Hencky strain at the failure point as the true strain and using that to calculate the true stress. In metals particularly, the simplifying assumption that the elastic strain can be subtracted from the overall strain to get plastic strain is used to find plastic strain, and the elastic region of the stress data is deleted. An example of the Hencky stress vs. strain curve is shown in Figure 4.3.

As the virtual strain gauge length in the DIC is 0.54 mm, element size in the gauge section is chosen to be less than 0.54 mm. The element size in the gauge section is 0.135 mm in the length direction and 0.27 mm in the length and width directions. Elements outside of the gauge section are cubic with size length 0.27 mm. The smaller edge length in the direction of the length of the gauge section is so that due to the ductility of the sample, the gauge length elements are close to cubes at the onset of necking. This means that in the

gauge section, 56 elements will fit in length, 10 elements will fit in the width, and 12 elements will fit through the thickness of the gauge section of the specimen.

The proportionality limit, or the stress where the stress and strain no longer have a linear relationship, is taken as the yield stress in the MAT-24 material model. The proportionality limit is used instead of the 0.2% offset yield stress due to the 0.2% offset yield stress overshooting the ideal yield stress for FEA applications as demonstrated in Figure 4.21.

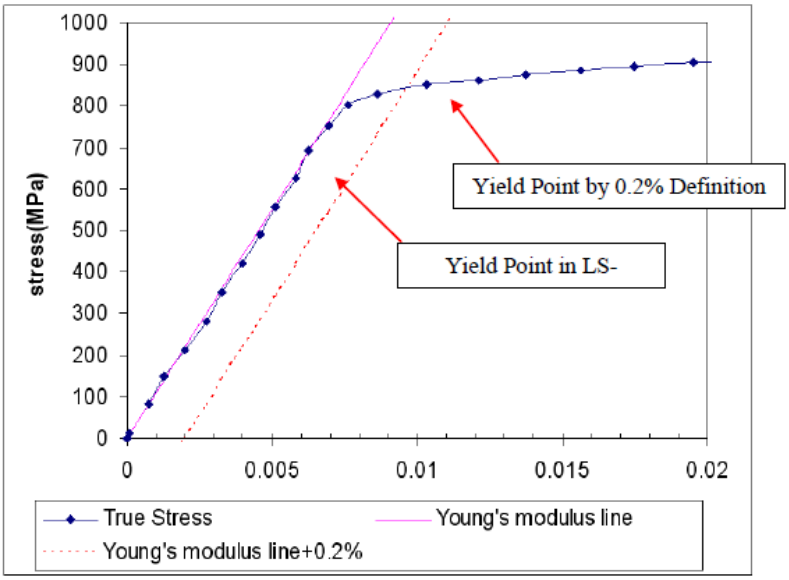

Figure 4.21: Differences in yield stress calculations for use in LS-DYNA simulations (Dolci *et al.* 2016).

The proportionality limit is taken as the yield stress, and the Hencky stress vs. strain curves are truncated before such that just the plastic region after the proportionality limit is reached is kept (all elastic strain is subtracted from the piecewise curve). This curve is taken as the true stress vs. plastic true strain curve.

The proportionality limit in a heat-treated sample (AM316L-HT-SR1-N1) is 221.8 MPa, and a material model is created from that data. The material model's

response is plotted against the response of the quasi-static actual tests as shown in Figure 4.22.

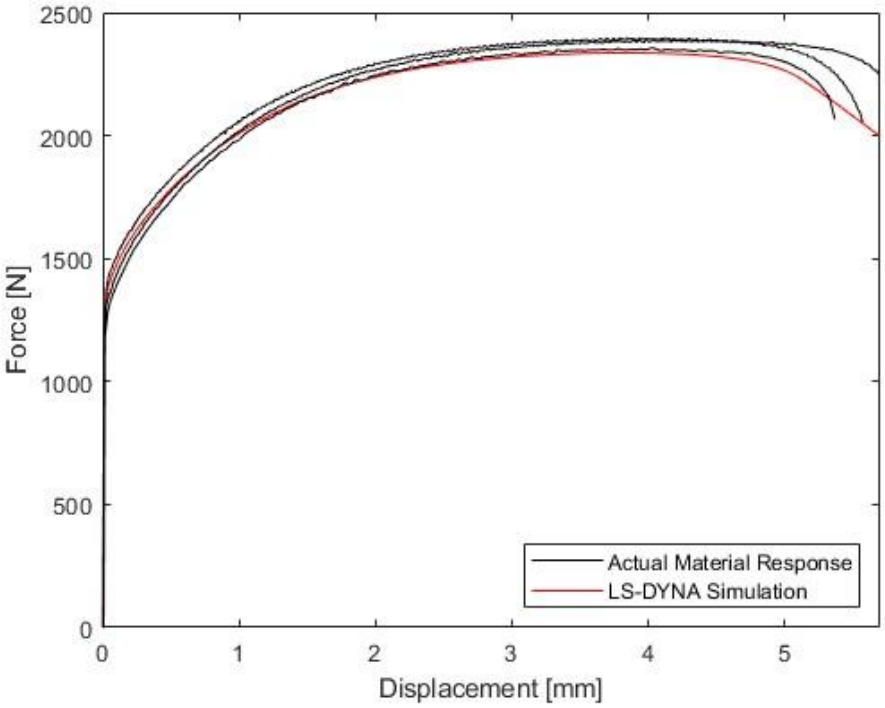

Figure 4.22: LS-DYNA MAT-24 heat-treated model compared to actual tests.

The results from the unmodified model created from the DIC Hencky stress vs. strain curves have similar force values at the same displacements and compare well to the actual tests. The necking behavior was able to be recreated due to fine elements in the model.

The as-built results showed a similar result when using the DIC Hencky strain from the quasi-static testing to create a model. AM316L-AB-SR1-N1 is used to create the model, and the proportionality limit found is 356.3 MPa. The model is created, and compared with the rest of the tests in Figure 4.23.

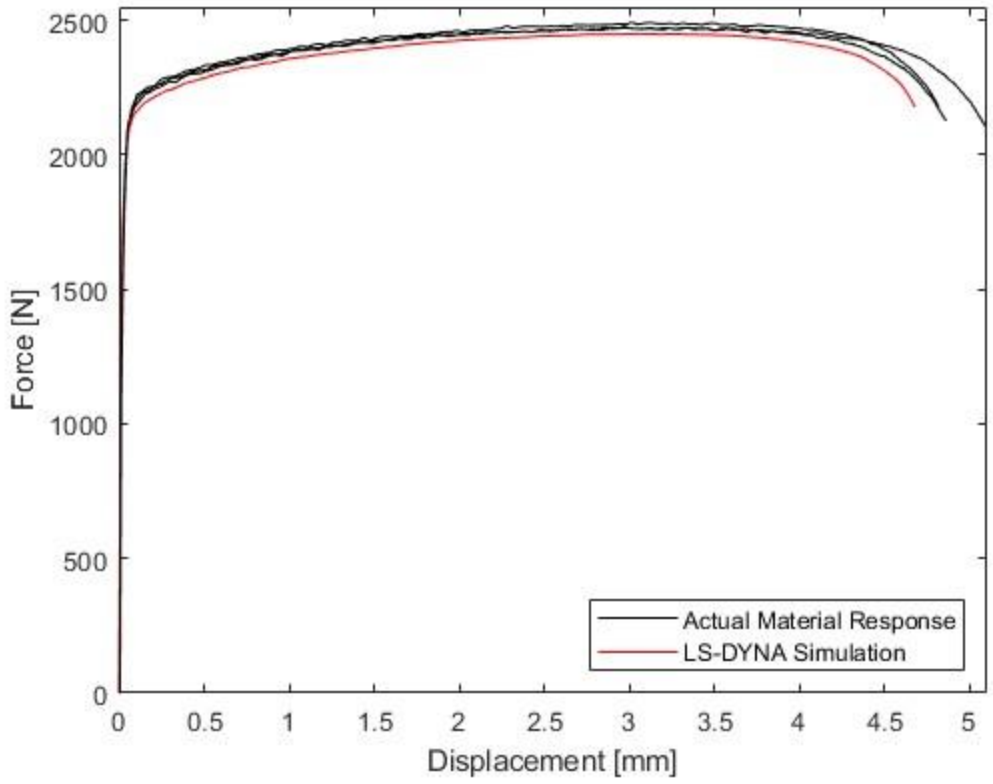

Figure 4.23: LS-DYNA MAT-24 as-built model compared to actual tests.

The model once again fits the results from the quasi-static testing well. However, the model through the whole test shows a slightly lower force reading of around 15 N (3 lbf or 0.6%) lower. The necking behavior was once again able to be recreated in the model due to the fine elements used.

4.5.2 0.2% Yield Stress as Material Model Yield Stress

Although taking the proportionality limit as the yield stress in the material model is preferred, using the 0.2% offset stress as the MAT-24 yield stress is also possible. However, a fitting function is required to make the model fit more closely when using the 0.2% offset yield stress. This method cuts off the DIC Hencky stress vs. strain curve at the 0.2% offset yield stress and uses the DIC Hencky curve past that point to be the true

stress vs. plastic true strain curve. This is expected to overshoot the stress values due to the yield stress being too high for this application.

In this method, the elements are set to be equal in size to the VSGL, or 0.54 mm cubes. This means that 14 elements will fit in length, 5 elements will fit in the width, and 3 elements will fit through the thickness of the gauge section of the specimen. The as-built results required editing of the inputted Hencky true stress vs. plastic true strain curve. Each stress value in the material model was multiplied by the function $f_{AB}(\epsilon) = -50.85\epsilon^6 + 90.2\epsilon^5 - 60.5\epsilon^4 + 18.65\epsilon^3 - 2.459\epsilon^2 + 0.04794\epsilon + 0.9775$ to get the data to fit the actual response, and the resultant data is shown in Figure 4.24.

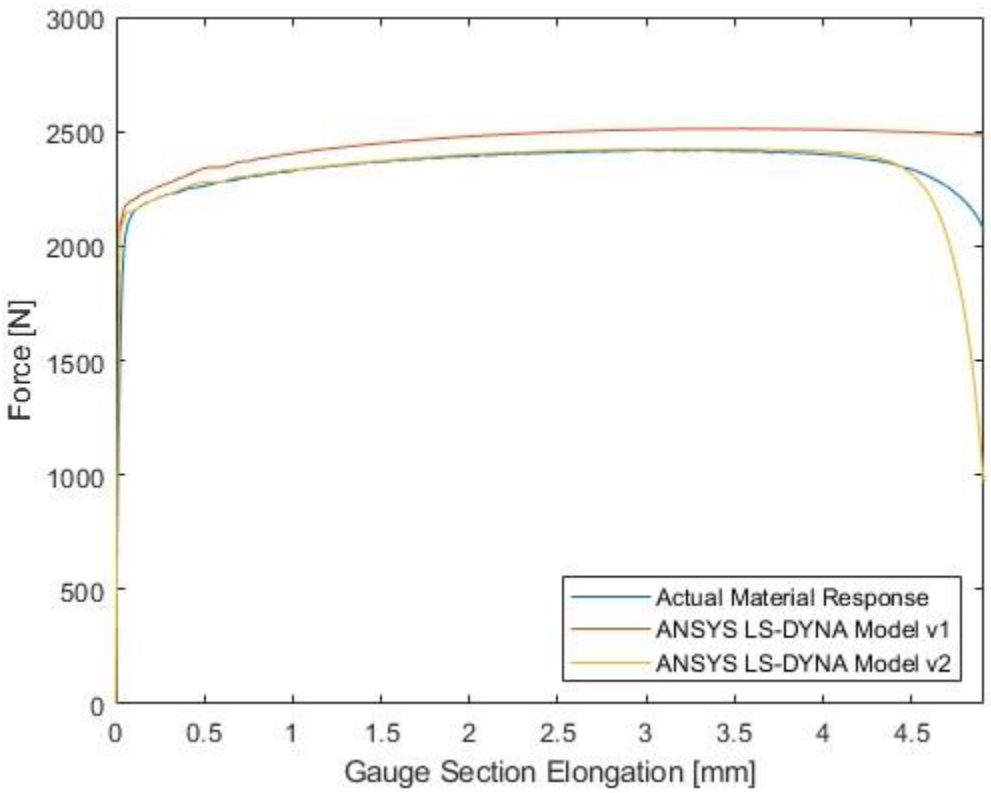

Figure 4.24: Comparison of AB quasi-static tension test and LS-DYNA simulated force vs. displacement.

The adjusted simulation results again line up well with the actual results except for the necking region, but overall line up much better than the initial assumption for the model.

This is due to some instability as the material begins to neck, where if a flow stress value in the material model is slightly too low, all strain will concentrate at that point, causing little deformation and a drastic decrease in force due to the Poisson effect.

The adjusting function is found by plotting the ratio of the experimentally determined mechanical force to the simulation force on the y-axis against the maximum plastic true strain on the x-axis, as shown in Figure 4.25.

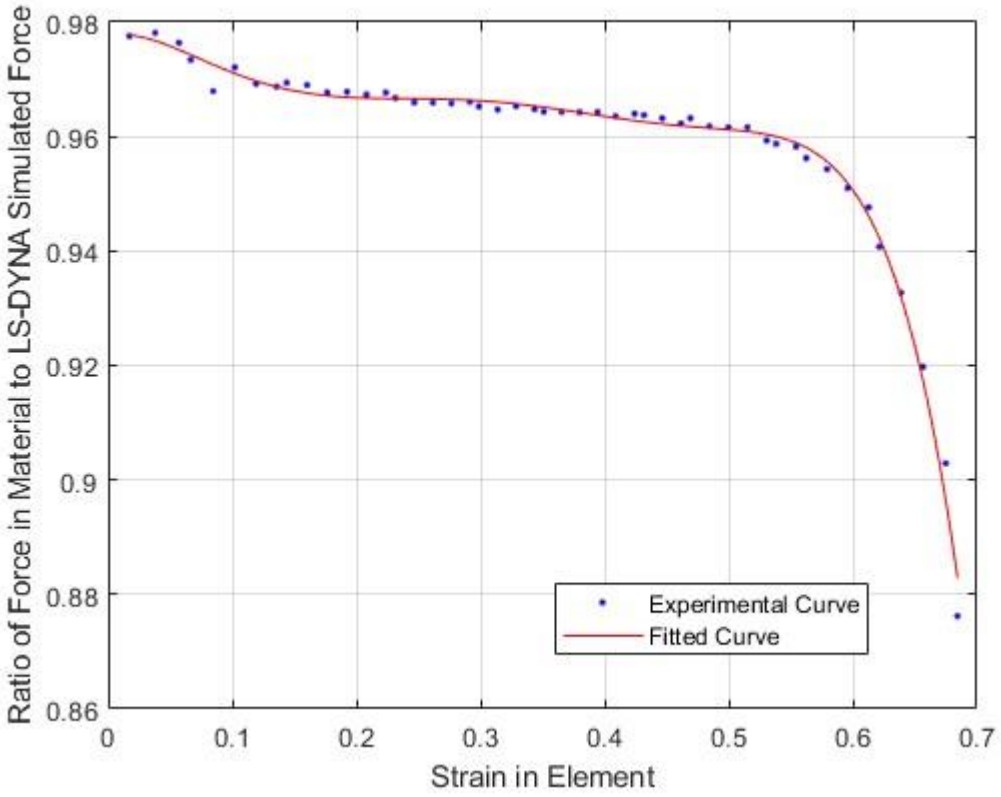

Figure 4.25: 6th order polynomial fitted to ratio of force in material to force in element plotted against elemental strain in simulation to correct error in material model in AB data.

The heat-treated material model using the unedited Hencky strain model resulted in a slightly incorrect model of the data, so a curve was fitted and each stress value is multiplied by a fitting function to correct the model as shown in Figure 4.26.

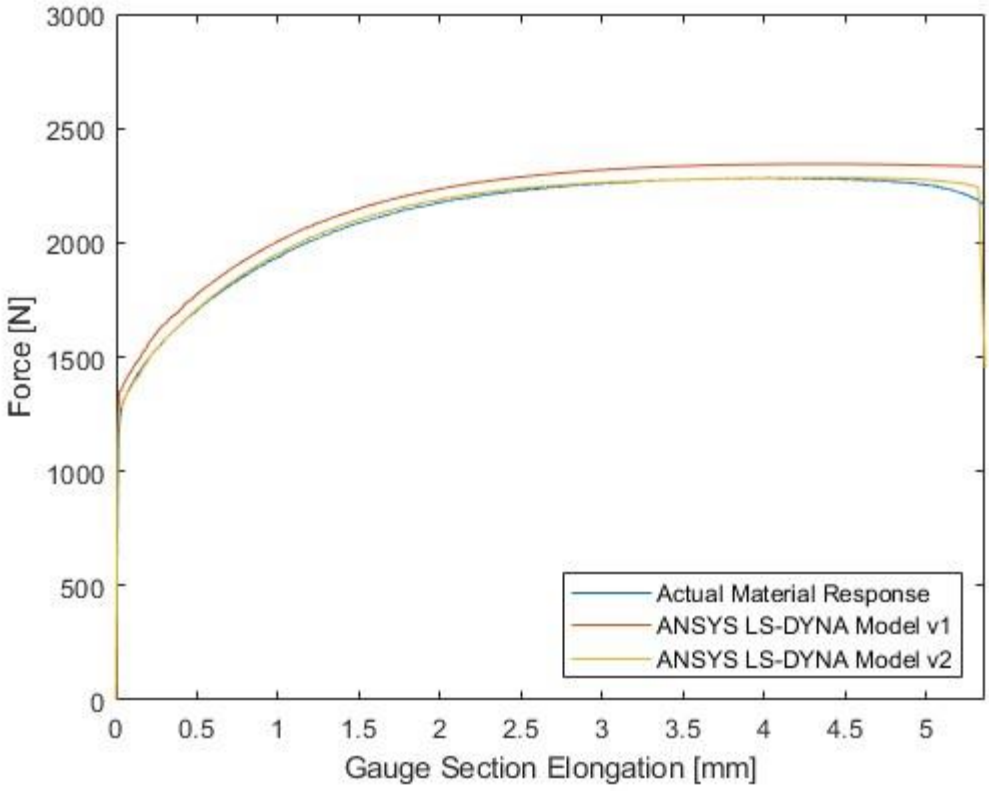

Figure 4.26: Comparison of HT quasi-static tension test and LS-DYNA simulated force vs. displacement.

The heat-treated curve fit the actual material response up until necking, where the model was unable to recreate the actual material response at that point.

The function that the heat-treated stress values in the material model is multiplied by is $f_{HT}(\epsilon) = -46.36\epsilon^6 + 88.52\epsilon^5 - 65.2\epsilon^4 + 23.29\epsilon^3 - 4.284\epsilon^2 + 0.04376\epsilon + 0.9467$, where $f_{HT}(\epsilon)$ is a factor for each stress level in the material element as a function of the strain in the element from the DIC Hencky strain model, and ϵ is the true plastic strain in the model.

This function is found in the same way and is shown in Figure 4.27.

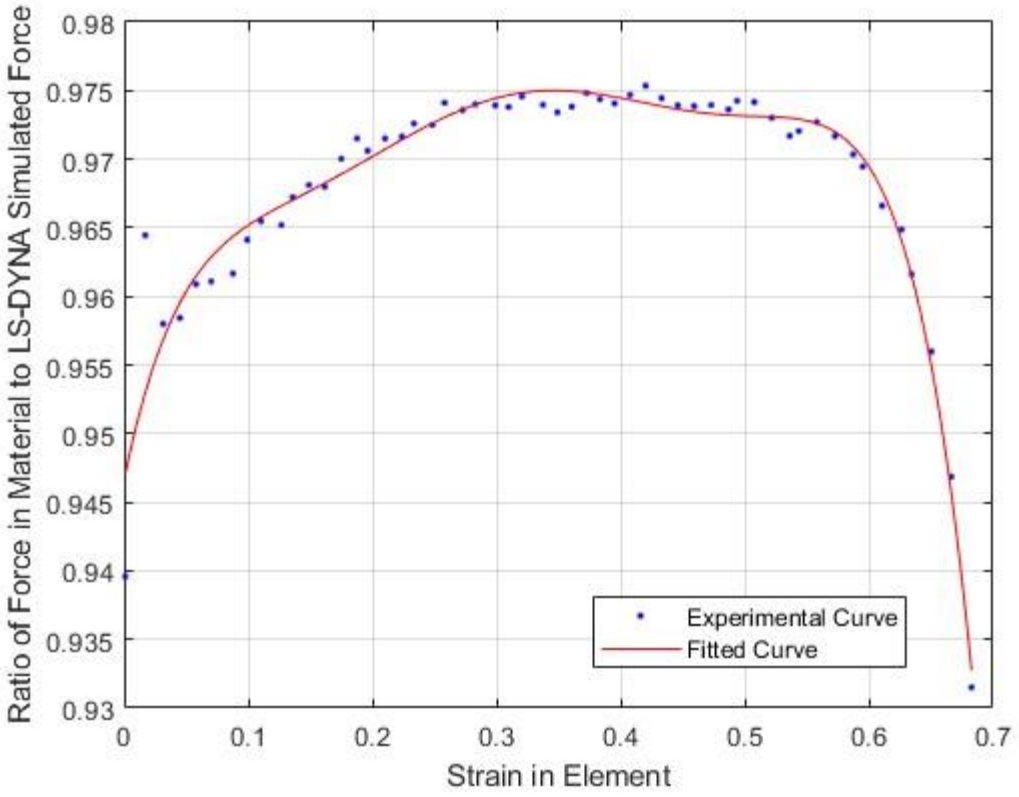

Figure 4.27: 6th order polynomial fitted to ratio of force in material to force in element plotted against elemental strain in simulation to correct error in material model in HT data.

As is demonstrated in Figure 4.22, Figure 4.23, Figure 4.24, and Figure 4.26, using the true DIC Hencky strain to create a material model is a more efficient method of creating a material model than the traditional "fan method" as shown in Figure 2.10 that is currently widely used. Taking the proportionality limit to be the yield stress creates a representative material model on the first try, but more analysis should be done when taking the 0.2% yield stress for the material model yield stress, but both methods are viable options.

4.6 Microstructural Analysis

Two samples that are from the quasi-static testing sequence are cut in the grip section and mounted in phenolic to view the microstructure. An as-built sample, AM316L-

AB-SR1-N2, and a heat-treated sample, AM316L-HT-SR1-N3, are sectioned at the grip section to view the build plane and the z-build direction to investigate the microstructure of the samples after building and the effects of heat treatment on the microstructure. After mounting, the samples are grinded using wet sandpaper from 220 grit up to 1200 grit to reduce the damage from cutting. At each grit level, the sample is examined to confirm scratch sizes in the sample are decreasing. The 1200 grit is the finest sandpaper used, and after this step, the samples are scratch free from the naked eye. The polishing process uses 1 μm aluminum oxide powder for 46 minutes or enough time where the scratches are no longer visible under a microscope. Finally, the samples are polished with a 0.05 μm aluminum oxide powder for 6 minutes. After the final polishing step, the microstructure is slightly visible under a microscope. A chemical etchant, Kalling's Reagent, is used to further reveal the microstructure in both the build plane and the z-build direction of the as-built and heat-treated sample. The optical microscopy (OM) images of the as-built samples show "X" scan pattern of laser during manufacturing and also many voids as shown in Figure 4.28.

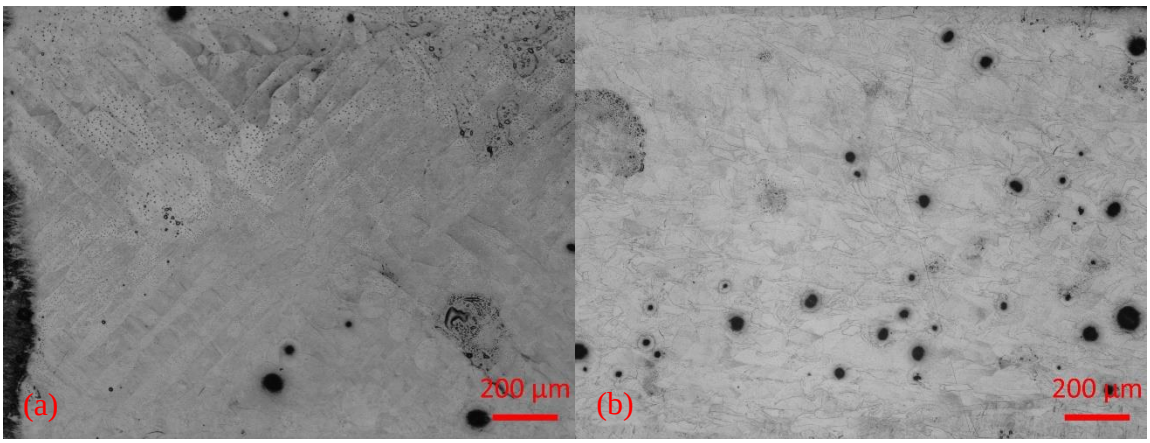

Figure 4.28: Representative 5x zoom picture of as-built samples of (a) build plane and (b) z-build direction.

The as-built results show remnants of the melt pools in build plane in the z-build direction. Porosity quantifications using ImageJ on Figure 4.28 (b) show a porosity of 0.381%, which is within the expected values. Due to the prevalence of melt pools that make individual grain boundaries hard to see, the grain sizes cannot be determined.

A heat-treated sample is also grinded, polished, and etched for viewing under an OM as shown in Figure 4.29. Grains can now be observed as the melt pool "X"-shaped boundaries have diffused.

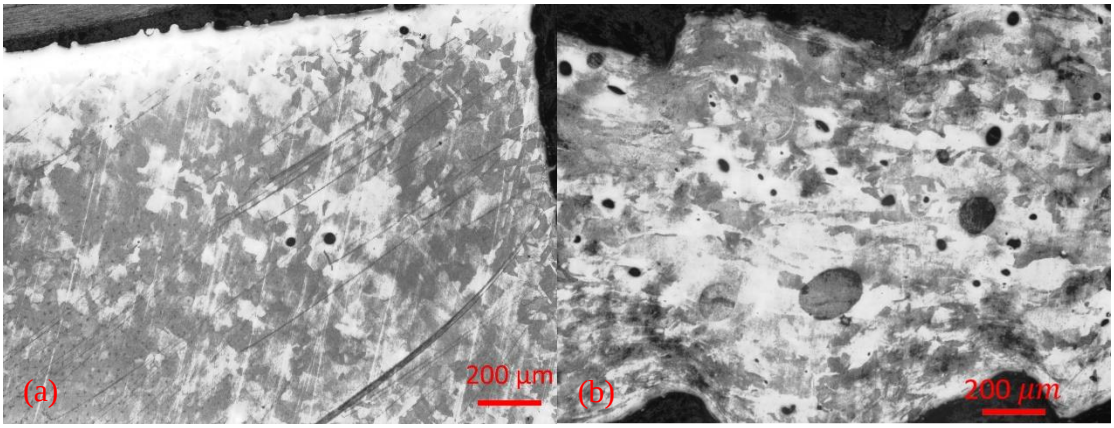

Figure 4.29: Representative 5x zoom picture of heat-treated samples of (a) build plane and (b) z-build direction.

The representative picture from the Figure 4.29 (b) shows a 0.358% porosity value using ImageJ, which is similar to the as-built part. The wave-like shapes on the edge of the samples are due to the grips slightly deforming the specimen. The porosities are relatively high, but are still within the prediction of Choi *et al.* (2016) of a <1.5% porosity.

Chapter 5. Conclusions and Future Work

Additive manufacturing is a newer process, and the parts that are made using additive manufacturing have unknown behavior due to the recent invention of the process. Therefore, quantifying the difference in behavior at high rates is necessary if the parts are to be used for military applications, airplanes, automotive vehicles, or anything else that experiences dynamic loading. Additionally, the differences between as-built samples of 316L stainless steel and heat-treated samples demonstrate how a basic homogenizing heat treatment affects the material properties of the AM material.

The heat-treated specimens demonstrate much more hardening behavior than the as-built specimens. This is possibly due to columnar grain shapes in the build direction in the as-built material allowing more room for dislocation motion before being impeded by a grain boundary, and therefore less work-hardening behavior. In the heat-treated, the grains have been recrystallized, and therefore are smaller and more homogenized, meaning dislocations will have less physical room to move in each grain. It is shown that both the heat-treated and the as-built specimens exhibit strain rate sensitivity, with a Johnson-Cook strain rate sensitivity parameter of $C = 0.0175$ and $C = 0.0163$, respectively. These values are within values found by other researchers for wrought 316L. The heat treatment dramatically altered material properties, decreasing the yield stress and increasing the amount of hardening that occurs in the plastic region after heat treatment.

The as-built displayed a much higher yield stress than its heat-treated counterpart. This could be due to the as-built part having higher residual stresses to impede the dislocations from moving as easily. The as-built part could potentially have more dislocations, as they have not been able to move towards each other and annihilate as they would have in a heat treatment. The defects in the as-built part on the microstructural level could also contribute to the decreased fracture strain in the as-built parts.

Using the DIC Hencky strain is shown to accurately and quickly allow the creation of material models for ANSYS LS-DYNA. The 0.2% offset yield stress can be taken as the yield stress in the material model, but due to this yield stress not being suitable for FEA applications, it requires a fitting function to adjust the material stress vs. strain curve to a lower yield stress value to accurately represent the material. Alternatively, taking the proportionality limit to be the yield stress allows the creation of an accurate material model without any additional modification of the material model on the first try.

Future work includes redesigning the specimen such that they will fracture under the current SHB test setup and loading pulse duration, or machining a longer striker bar such that it could provide a sufficiently long pulse to fracture the sample. Also, investigating methods to reduce the oscillations in the incident wave will be performed. The oscillations repeatedly degraded the quality of the data, and modifying the test setup such as by using a pulse shaper could help to limit the oscillations in the incident wave.

Future work also includes more research into the microstructural differences between the AB and HT materials to determine the underlying causes behind the observed differences in behaviors occur in order to better predict the differences in the future. This

will be useful for analyzing new manufacturing processes or heat treatments, and how such process will affect the microstructure and mechanical properties.

References

"AISI Type 316L Stainless Steel, Annealed Bar." *MatWeb*, www.matweb.com/search/DataSheet.aspx?MatGUID=a2d0107bf958442e9f8db6dc9933fe31&ckck=1. Accessed 16 Feb. 2024.

Ahmed, Nissar, *et al.* "Process parameter selection and optimization of laser powder bed fusion for 316l Stainless Steel: A Review." *Journal of Manufacturing Processes*, vol. 75, 2022, pp. 415–434, https://doi.org/10.1016/j.jmapro.2021.12.064.

Anderson, Scott. "SHPB Tension Testing with REL's Dynamic Materials Testing System." Mar. 2020.

"ASTM Standard A240/A240M." *ASTM International*, vol. 23, 2 June 2023, https://doi.org/10.1520/A0240_A0240M-23.

Atkinson, H V, and S Davies. "Fundamental aspects of hot isostatic pressing: An overview." *Metallurgical and Materials Transactions A*, vol. 31, no. 12, 2000, pp. 2981–3000, https://doi.org/10.1007/s11661-000-0078-2.

"Calibration Using VIC-Snap & VIC-3D." *Correlated Solutions Digital Image Correlation*, 9 June 2022, www.correlatedsolutions.com/training-videos/v/calibration-tutorial.

Choi, Joon-Phil, *et al.* "Densification behavior of 316l stainless steel parts fabricated by selective laser melting by variation in laser energy density." *Materials*

Transactions, vol. 57, no. 11, 14 Oct. 2016, pp. 1952–1959, https://doi.org/10.2320/matertrans.m2016284.

Ding, Donghong, *et al.* "Wire-feed additive manufacturing of metal components: Technologies, Developments and future interests." *The International Journal of Advanced Manufacturing Technology*, vol. 81, no. 1–4, 2015, pp. 465–481, https://doi.org/10.1007/s00170-015-7077-3.

Dolci, Stefano, *et al.* "Incorporation of Inconel-718 Material Test Data into Material Model Input Parameters for *MAT_224." *Dyna Look*, 2016, www.dynalook.com/conferences/14th-international-ls-dyna-conference/aerospace/incorporation-of-inconel-718-material-test-data-into-material-model-input-parameters-for-mat_224.

Dossett, Jon L, and George E Totten. "Steel Heat Treating Fundamentals and Processes." *ASM Handbook*, vol. 4A, 30 Aug. 2013, https://doi.org/10.31399/asm.hb.v04a.9781627081658.

Garcia-Colomo, Alberto, *et al.* "A comparison framework to support the selection of the best additive manufacturing process for specific aerospace applications." *International Journal of Rapid Manufacturing*, vol. 9, no. 2/3, 2020, p. 194, https://doi.org/10.1504/ijrapidm.2020.107736.

Gel'atko, Matúš, *et al.* "Stress relieving heat treatment of 316L stainless steel made by additive manufacturing process." *Materials*, vol. 16, no. 19, 28 Sept. 2023, p. 6461, https://doi.org/10.3390/ma16196461.

Gilat, Amos. “Torsional Kolsky Bar Testing.” *Mechanical Testing and Evaluation*, vol. 8, 2000, pp. 505–515, https://doi.org/10.31399/asm.hb.v08.a0003300.

Gu, Dongdong, and Yifu Shen. “Balling phenomena in direct laser sintering of stainless steel powder: Metallurgical mechanisms and control methods.” *Materials & Design*, vol. 30, no. 8, 2009, pp. 2903–2910, https://doi.org/10.1016/j.matdes.2009.01.013.

Güden, Mustafa, *et al.* “The strain rate sensitive flow stresses and constitutive equations of a selective-laser-melt and an annealed-rolled 316L Stainless Steel: A comparative study.” *Materials Science and Engineering: A*, vol. 838, Mar. 2022, p. 142743, https://doi.org/10.1016/j.msea.2022.142743.

Hammer, Jeremiah Thomas. “Plastic Deformation and Ductile Fracture of Ti-6al-4v under Various Loading Conditions.” *The Ohio State University*, 2012.

Hoggatt, C. R, and R. F Recht. “Stress-strain data obtained at high rates using an expanding ring.” *Experimental Mechanics*, vol. 9, no. 10, 1969, pp. 441–448, https://doi.org/10.1007/bf02410405.

Hopkinson, Bertram. “A method of measuring the pressure produced in the detonation of high explosives or by the impact of Bullets.” *Proceedings of the Royal Society of London. Series A, Containing Papers of a Mathematical and Physical Character*, vol. 89, no. 612, 1914, pp. 411–413, https://doi.org/10.1098/rspa.1914.0008.

Johnson, Gordon R., and William H. Cook. “Fracture characteristics of three metals subjected to various strains, strain rates, temperatures and pressures.” *Engineering Fracture Mechanics*, vol. 21, no. 1, Jan. 1985, pp. 31–48, https://doi.org/10.1016/0013-7944(85)90052-9.

Kamath, Chandrika, *et al.* “Density of additively-manufactured, 316L SS parts using laser powder-bed fusion at powers up to 400 W.” *The International Journal of Advanced Manufacturing Technology*, vol. 74, no. 1–4, 2014, pp. 65–78, https://doi.org/10.1007/s00170-014-5954-9.

Kolsky, Herbert. “An investigation of the mechanical properties of materials at very high rates of loading.” *Proceedings of the Physical Society. Section B*, vol. 62, no. 11, Nov. 1949, pp. 676–700, https://doi.org/10.1088/0370-1301/62/11/302.

Liu, Yude, *et al.* “Study on performance optimization of 316L stainless steel parts by high-efficiency selective laser melting.” *Optics & Laser Technology*, vol. 138, 2021, https://doi.org/10.1016/j.optlastec.2020.106872.

“LS-DYNA® KEYWORD USER’S MANUAL.” Livermore Software Technology Corporation, 27 Sept. 2021.

Onaka, Susumu. “Appropriateness of the hencky equivalent strain as the quantity to represent the degree of severe plastic deformation.” *MATERIALS TRANSACTIONS*, vol. 53, no. 8, 2012, pp. 1547–1548, https://doi.org/10.2320/matertrans.m2012077.

Rai, R, *et al.* "Heat transfer and fluid flow during keyhole mode laser welding of tantalum, ti–6al–4v, 304L stainless steel and Vanadium." *Journal of Physics D: Applied Physics*, vol. 40, no. 18, 2007, pp. 5753–5766, https://doi.org/10.1088/0022-3727/40/18/037.

Rodrigues, Pedro Henrique, *et al.* "Effect of hot isostatic pressing of water atomized Aisi 316L manufactured by Laser Powder Bed Fusion." *Materials Research*, vol. 26, no. suppl 1, 2023, https://doi.org/10.1590/1980-5373-mr-2023-0074.

Schneider, Judith. "Introduction to Microscopy and OM." MAE577 Class Lecture. MAE577 Class Lecture, 2023.

Seidt, J.D., and A. Gilat. "Plastic deformation of 2024-T351 aluminum plate over a wide range of loading conditions." *International Journal of Solids and Structures*, vol. 50, no. 10, 2013, pp. 1781–1790, https://doi.org/10.1016/j.ijsolstr.2013.02.006.

Seidt, Jeremy Daniel. "Plastic Deformation and Ductile Fracture of 2024-T351 Aluminum under Various Loading Conditions." Ohio State University, 2010.

Taylor, Geoffery. "The use of flat-ended projectiles for determining dynamic yield stress." *Proceedings of the Royal Society of London. Series A. Mathematical and Physical Sciences*, vol. 194, no. 1038, 1948, pp. 289–299, https://doi.org/10.1098/rspa.1948.0081.

Umbrello, D., *et al.* "The influence of Johnson–Cook material constants on finite element simulation of machining of Aisi 316L Steel." *International Journal of*

Machine Tools and Manufacture, vol. 47, no. 3–4, Mar. 2007, pp. 462–470, https://doi.org/10.1016/j.ijmachtools.2006.06.006.